EXAMINATION OF IRON UNDERSATURATION IMPACT ON FLOW ACCELERATED CORROSION IN THE CANDU-6 PRIMARY HEAT TRANSPORT SYSTEM

by

Jessica Ashley Gauthier

BScE in Chemical Engineering, University of New Brunswick, 2018

A Thesis Submitted in Partial Fulfillment
of the Requirements for the Degree of

Master of Science in Engineering

in the Graduate Academic Unit of Chemical Engineering

Supervisors: William Cook, PhD, Chemical Engineering
Craig Stuart, PhD, Canadian Nuclear Laboratories

Examining Board: Brian Lowry, PhD, Chemical Engineering, Chair
Guida Bendrich, PhD, Chemical Engineering
Olga Palazhchenko, PhD, Chemical Engineering
Clodualdo Aranas, PhD, Mechanical Engineering

This thesis is accepted by the
Dean of Graduate Studies

THE UNIVERSITY OF NEW BRUNSWICK

March, 2023

ABSTRACT

The rate of corrosion can be mitigated by maintaining optimum chemistry conditions and selecting a compatible material for the system environment. Corrosion mitigation is a significant concern across all industries, as fostering an adequate corrosion mitigation program promotes optimum performance, as well as preventing the release of system process fluids into the environment, which is particularly important within the nuclear industry.

From the investigation of the Point Lepreau Nuclear Generating Station (PLNGS) data regarding changes in flow accelerated corrosion (FAC) rate when a fresh lithiated resin column is put into service, it appears that the increase in FAC rate is consistent and was even present prior to the feeder replacement during the 2008 to 2012 refurbishment. Examining this phenomenon further, it appears that the quantity of lithium that is released from the lithiated resin during service could be an indication of the quantity of iron corrosion products being removed by the resin bed as it closely correlates with the changes in the measured FAC rate.

The testing program presented here directly examined the effects of changing purification rate on the corrosion rate observed on carbon steel feeder material exhibiting FAC. Over the duration of approximately two years, CNER's Loop 1 was reconfigured from a once-through configuration to a recirculating loop, complete with a high-temperature pump. This recirculating configuration more accurately represents the CANDU Primary Heat Transport System (PHTS)[1] in terms of simulating inlet feeder and outlet feeder

[1] Registered to AECL

operational temperatures and overall chemistry conditions and allowed for the provision of side-stream purification.

Three sets of experiments were performed and confirmed the direct correlation between the test loop's purification flow rate and the FAC rate observed on the test probes. Also of note from the experiments was the surprisingly high amount of magnetite deposition observed on the particulate filters, particularly in the high-temperature recirculating section of the loop. The entire test loop is constructed of 316 SS and the only carbon steel present is from the small-bore electrical resistance probe and hydrogen effusion probe located in the test section, representing a small fraction of the overall surface area. It was not expected that significant iron corrosion products would be present or observed from just the test probes alone; thus, a set of "sacrificial" carbon steel tubes with similar dimensions to the monitoring probes were fabricated and installed. They were never used due to both the unexpected high amount of corrosion products observed in the system and in limitations of the high-temperature recirculating pump.

The observed correlation between increased purification flow and increased FAC rates as determined from the loop tests has been confirmed by comparing the experimental results to prior modelling work, which showed a similar trend. Consistent and reproducible correlations were observed from the testing program with nominally identical impact, as evidenced by the slope of the regression curve. While the modelling results show a similar trend, the fact that the modelled change in FAC rate is only about half the magnitude of the observed change from the loop tests potentially indicates that our understanding of total circulating iron and its impact on corrosion and chemistry in the PHTS is still lacking.

DEDICATION

I dedicate this work to all the women in STEM who paved the way before me, and to those who will follow.

May we know them.

May we be them.

May we raise them.

ACKNOWLEDGEMENTS

Firstly, I would like to acknowledge several organisations that made this work possible; the CANDU Owners Group, Chemistry Materials and Components Technical committee and Chemistry Working Group (under Work Package 40186), as well as the Natural Sciences and Engineering Research Council and the University Network of Excellence in Nuclear Engineering. This work would not have been possible without the funding they provided. In addition, the Canadian Nuclear Laboratories is also recognised for their generous donation of a magnetically driven pump, which played an integral part in making Loop-1 operational and fit for this research.

I would like to acknowledge both of my supervisors for providing me with exceptional support, encouragement, and oversight over the duration of this work. Willy has supported me in my academic development towards nuclear energy since undergrad, and for that I am thankful. The staff at CNER and the Chemical Engineering Department; Brad McCann; Chester Morris; Dr. Olga Palazhchenko; Adon Briggs, and Carl Murdock, are appreciated for their support over the course of this work. I am thankful for the support Brad and Chester provided throughout the design, construction, and operation phases. I've crossed paths with Olga numerous times over my academic career. I am thankful for her support not only as a colleague and a mentor, but also as a friend. To Adon and Carl, I am thankful for not only all the support provided in regard to purchasing, mechanical maintenance, machining, etcetera, but also for the many hours spent in the mechanical shop teaching.

I am thankful for my life long best friends, Brianna and Chelsie, for pretending that they had any idea of what I was talking about when I would come home ranting about my

system not working, and for always choosing to love me, even when I let the stress consume me. Finally, I am thankful for the unconditional love and support my parents have provided me. I would not be where I am today without them.

Table of Contents

List of Tables

List of Figures

Nomenclature

A_{Cross}	Cross-sectional area (m^2)
A_{Diff}	Diffusion area of hydrogen through carbon steel (cm^2)
a_{H^+}	Activity of the hydrogen ions in the solution
$a_{oxidized}$	Activity of oxidized species
$a_{reduced}$	Activity of reduced species
C	Total concentration in the liquid solution $\left(\frac{mol}{kg\ D_2O}\right)$
C_b	Concentration of iron in the bulk fluid $\left(\frac{mol}{kg\ D_2O}\right)$
C_{sat}	Saturation concentration of iron $\left(\frac{mol}{kg\ D_2O}\right)$
c	Stoichiometric molar concentration of the solution
c_A	Concentration of the exchange-ion in the liquid $\left(\frac{mol}{kg\ D_2O}\right)$
c_B	Concentration of the counter-ion in the liquid $\left(\frac{mol}{kg\ D_2O}\right)$
c_i	Concentration of the ion $\left(\frac{mol}{cm^3}\right)$
d	Distance (cm)
E_{act}	Actual potential (Volts)
E_{eq}	Equilibrium potential (Volts)
E°	Standard potential (Volts)
F	Faraday's constant $\left(96485.3\ \frac{C}{mol}\right)$
K_A	Selectivity of the exchange-ion
K_B	Selectivity of the counter-ion
K_w	Dissociation constant of water
k	Mass transfer constant $\left(\frac{cm}{s}\right)$
k	Specific conductance of the solution $\left(\frac{S}{m}\right)$
k_i	Specific conductance of the ion $\left(\frac{S}{cm}\right)$
M_{Fe}	Molecular weight of iron $\left(55.85\ \frac{g}{mol}\right)$

$\dot{m}$	Flow accelerated corrosion rate $\left(\frac{\mu m}{a}\right)$
m_{H^+}	Concentration of the hydrogen ions $\left(\frac{mol}{kg}\right)$
m^o	Activity of the standard reference state $\left(1\frac{mol}{kg}\right)$
n	Number of electrons transferred
Q	Total capacity $\left(\frac{mol}{kg\ Resin}\right)$
q_{AR}	Concentration of the exchange-ion in the resin $\left(\frac{mol}{kg\ Resin}\right)$
q_{BR}	Concentration of the counter-ion in the resin $\left(\frac{mol}{kg\ Resin}\right)$
R	Universal gas constant $\left(8.314\frac{m^3\ Pa}{mol\ K}\right)$
R	Resistivity (mW)
r_o	Outer radius of ERP (cm)
T	Temperature (K)
t_{wall}	Wall thickness of ERP (cm)
Λ_m	Molar conductivity $\left(\frac{S\ cm^2}{mol\ eq}\right)$
$\gamma_{\pm}$	Ionic activity coefficient
$\frac{\delta P_{H_2}}{\delta t}$	Production rate of hydrogen gas $\left(\frac{Pa}{day}\right)$
$\frac{\delta n_{H_2}}{\delta t}$	Production rate of hydrogen $\left(\frac{mol_{H_2\,(g)}}{day}\right)$
$\lambda_{m,i}$	Molar conductivity on the ion $\left(\frac{S\ cm^2}{mol\ eq}\right)$
ρ_{Fe}	Density of iron $\left(7.87\ \frac{g}{cm^3}\right)$
ΔG°_{rxn}	Standard Gibb's free energy of reaction $\left(\frac{J}{mol}\right)$
ρ(T)	Specific resistivity (mW-cm)

Abbreviations

AECL	Atomic Energy of Canada Limited
CANDU	Canadian Deuterium-Uranium
CNER	Centre for Nuclear Energy Research
CNL	Canadian Nuclear Laboratories
COG	CANDU Owners Group
CS	Carbon Steel
ERP	Electrical Resistance Probe
F	Filter
FAC	Flow Accelerated Corrosion
FWT	Feeder Wall Thinning
H	Heater
HEPro	Hydrogen Effusion Probe
HX	Heat-Exchange
IX	Ion-Exchange
OPEX	Operating Experience
P	Pump
PHTS	Primary Heat Transport System
PHWR	Pressurized Heavy Water Reactors
PLNGS	Point Lepreau Nuclear Generating Station
SCS	Sacrificial Carbon Steel
SHE	Standard Hydrogen Electrode
SMR	Small Modular Reactor
UNB	University of New Brunswick

1 Introduction

Electricity is an essential need that is often taken for granted; in the best of times, society struggles when faced with unforeseen power outages. Modern society has evolved to be highly dependent on reliable electricity. In addition to maintaining and upgrading existing generating stations to higher outputs, growing global energy demands require more generating stations to be brought on-line in a carbon-free way. While electricity has drastically improved the quality of human life, a high dependency on fossil fuels since the industrial revolution has resulted in the current climate crisis.

With a high energy density and amongst the lowest life-cycle carbon emissions, nuclear power is undeniably the superior technology in regard to reliable, clean energy. As of May 2020, there are 440 nuclear reactors operating across the globe, and 55 in the construction phase [1]. Pressurized Water Reactors (PWR) make up the bulk of reactors in operation, followed by Boiling Water Reactors (BWR) and Pressurized Heavy Water Reactors (PHWR), which are also known as the Canada Deuterium-Uranium (CANDU) reactor. The newest generation of nuclear reactors, the Small Modular Reactor (SMR), are currently in the design and approval phases. While SMR designs will address the significant capital costs associated with conventional reactor technologies, reduce legacy waste via fuel re-processing, and provide a promising outlook for the global nuclear industry, SMRs will not reach the construction phase for at least another decade. In the meantime, it is essential that the nuclear industry continues to collaborate, share operational experiences, and continue to prioritize maintaining existing reactors — well maintained and refurbished units can operate significantly longer than their original life expectancy, thus further reducing their life-cycle carbon emissions.

Corrosion mitigation is a common practice across all industries, and is essential for maintaining healthy, long-lived systems that will perform as desired — as well as preventing the release of unwanted substances into the environment due to system failures. Corrosion mitigation is a billion-dollar industry, where mitigation generally begins during the design phase. Design engineers assess expected process conditions for a given system in order to select compatible materials for construction. Consideration is given to: the material's ability to form an oxide-film in the given environment (see Section 2.2); material cost; and in the case of the nuclear industry, the material's properties when exposed to a radiation field and neutron flux (see Section 2.1.3). Unfortunately, the performance of a selected material is only as good as the information available, as was the case for the carbon steel outlet feeder pipes originally selected for the CANDU reactor (see Section 2.1).

Following a routine maintenance outage in the mid 90's, a unit in the CANDU fleet was forced to cease start-up actitivites due to the presence of foregin material in the primary heat transport system. Investigation of the incident eventually concluded that this particular unit, and all other CANDU units, were experiencing unforeseen outlet feeder pipe wall thinning [2]. In addition, it was also concluded that the excessive wall thinning was a consequence of the outlet feeders experiencing significantly higher flow accelerated corrosion (FAC) rates than what was predicted during the design phase and original material compatability testing.

The Canadian nuclear industry had since launched a series of collaborative research activities to better understand the excessive outlet feeder wall thinning and develop strategies to mitigate it. While research activities have produced strategies to mitigate the rate of feeder wall thinning such as increasing the chromium content of the carbon steel

from 0.02% to 0.33% during replacement or refurbishment activities, research efforts have yet to identify whether FAC in the outlet feeder pipes is governed exclusively by a mass transfer or by combination with magnetite dissolution. Recent data from a Canadian CANDU unit suggests that FAC in the outlet feeder pipes is driven by magnetite dissolution, and that this may be significantly influenced by the purification half-life of the primary heat transport system (PHTS - see Section 2.1).

With some uncertainty still surrounding the driving force mechanism, the objective of this work was to:

- Demonstrate that the operation of the PHTS purification system, which was previously thought to have no effect on FAC, plays a significant role
- Optimize operation of the purification system to minimize FAC rate while achieving other system requirements such as minimizing activity transport throughout the PHTS.

The results from the work may ultimately serve as a stepping stone for improving existing FAC models at UNB's Centre of Nuclear Energy Research (CNER). Other supporting work at CNER is also underway such as re-evaluating industry standards for solubility of iron species such as the classic work by Tremaine and LeBlanc [3].

2 Literature Review

2.1 The CANDU Reactor

2.1.1 Development and Existing Reactor Overview

While World War II is a dark chapter in Mankind's history, the development of the atomic bomb facilitated innovation within Canada that would eventually lead to the birth of the CANDU reactor — where Canada's newfound experience in manufacturing and utilizing heavy water (D_2O) as a moderator became essential to developing a reactor that utilizes natural Uranium as a fuel source. Since World War II, Canada has continued to be a major contributor to the nuclear industry and the development of nuclear technologies. The CANDU reactor is a unique and attractive reactor design — representing approximately 12 % of nuclear reactors operating worldwide and is currently the exclusive nuclear reactor technology within Canada [4].

The Canadian fleet consists of nineteen CANDU reactors located in the provinces of Ontario and New Brunswick, where 18 units are distributed across 3 sites in Ontario, leaving 1 unit at the Point Lepreau Nuclear Generating Station (PLNGS) in New Brunswick, as described in Table 2.1-1. This thesis focuses on the operating reactors within the CANDU^6 fleet, with a specific emphasis on the PLNGS unit [5].

Table 2.1-1. Summary of Operational CANDU Reactors in Canada. [5]

Unit [Model]	Construction Start [Grid Connection]	Unit [Model]	Construction Start [Grid Connection]
BRUCE-1 [791]	1971 [1977]	DARLINGTON-3 [850]	1984 [1992]
BRUCE-2 [791]	19 70 [1976]	DARLINGTON-4 [850]	1985 [1993]
BRUCE-3 [750A]	1972 [1977]	PICKERING-1 [500A]	1966 [1971]
BRUCE-4 [750A]	1972 [1978]	PICKERING-4 [500A]	1968 [1972]
BRUCE-5 [750B]	1978 [1984]	PICKERING-5 [500B]	1974 [1982]
BRUCE-6 [750B]	1978 [1984]	PICKERING-6 [500B]	1975 [1983]
BRUCE-7 [750B]	1979 [1986]	PICKERING-7 [500B]	1976 [1984]
BRUCE-8 [750B]	1979 [1987]	PICKERING-8 [500B]	1976 [1986]
DARLINGTON-1 [850]	1982 [1990]	POINT LEPREAU [6]	1975 [1982]
DARLINGTON-2 [850]	1981 [1990]		

2.1.2 Unexpected FAC in the Primary Heat Transport System

During an extended maintenance outage in 1995-96, a heavy water leak forced PLNGS to cease initial start-up attempts due to a crack in one of the PHTS outlet feeder pipes (feeder S08) which required replacement prior to resuming start-up activities. Analysis of feeder S08 at the Chalk River Laboratories (CRL) found significant thinning of the outlet feeder wall and the formation of scallops on the inner surface of the pipe *between the reactor face and the first bend*, indicating FAC was the predominant mechanism. The presence of scallops suggest that the corrosion process is driven by the dissolution of iron — which is directly related to the solubility of iron at PHTS operating conditions [2]. Routine ultrasonic feeder pipe wall thickness measurements — *taken at easily assessable*

points away from the first bend and away from the reactor face — provided no prior evidence that the outlet feeders in the PLNGS unit were experiencing excessive wall thinning. Following the analysis of feeder S08, a thorough feeder wall thickness survey at PLNGS — measuring between the first bend and the reactor face — concluded that the outlet feeder pipes were indeed experiencing significant rates of wall thinning [6].

The findings from PLNGS were worrisome and quickly prompted thorough feeder wall thickness surveys across the CANDU fleet. Results from all CANDU sites, both domestic and abroad, consistently found that the outlet feeder pipes were experiencing far greater rates of wall thinning than were anticipated for the feeder piper material (A106 Gr.B carbon steel). All CANDU sites also consistently reported that the inlet feeder pipes were not experiencing wall thinning [2].

In the case of PLNGS, corrosion rates greater than 120 µm/a[2] had been measured, while only 10-20 µm/a were anticipated as per material compatibility testing during the design phase [2]. The excessive feeder wall thinning forced PLNGS to replace at least a dozen outlet feeder pipes prior to the reactor's midlife refurbishment. The estimated costs associated with premature outlet feeder pipe replacement is in the range of tens of millions, which factors in costs associated with bringing the reactor off-line during replacement activities [7].

In response to the unexpected feeder thinning rates, the Canadian nuclear industry through the CANDU Owners Group (COG) launched the Feeder Integrity Joint Project (FIJP) to investigate and mitigate excessive rates of feeder wall thinning in both existing

[2] µm/a = micrometers annually

and future reactor designs. COG collaborated with various organizations, including the Atomic Energy of Canada Limited (AECL), CNER and UNB Nuclear to investigate the phenomenon.

The absence of excessive wall thinning in the inlet feeder pipes coupled with the presence of scallops in the outlet feeders suggested that the undersaturation of iron in the outlet feeders is a major driver in the FAC mechanism (see Section 2.3). Through the course of investigation through the FIJP, the FAC mechanism is thought to be quite well understood and was able to identify methods of mitigating feeder FAC by marginal increases of the chromium content in the carbon steel (CS) feeder pipes from 0.02% (CS A106B) to 0.33% (CS A106C), as well as narrowing chemistry specifications to maintain tighter pH control in the PHTS [8].

Another outcome of the FIJP was the development of the electrical resistance probe (ERP) and hydrogen effusion probe (HEP) on-line corrosion monitors. Corrosion of carbon steel under PHTS system conditions results in the formation of hydrogen gas that diffuses to the outer surface of the carbon steel pipe. The HEP monitors the hydrogen production rate, which is then used to determine FAC rate using the mass balances of the process (see Section 3.3.2)

CNER was tasked with determining if the initially laboratory-base HEP corrosion monitoring tool could be ported to an operating CANDU. CNER installed the first industrial HEPro at PLNGS in 2006, and another at Darlington in March 2020 while the station was completing mid-life refurbishment activities. Since its initial installation at PLNGS, the HEPro has collected valuable data with regards to understanding FAC during normal operation and start-up procedures. The HEPro was initially installed at PLNGS on outlet feeder pipe (C-11) on the vertical section of piping following the initial bends. After

PLNGS's midlife refurbishment where all A106B feeders were replaced with grade A106C carbon steel with 0.33% chromium, the HEPro was reinstalled in the same location — however, due to electronic equipment malfunctions it was not placed in full service after the initially hot condition process (Sept 2012) until 2016 [7]. From 2016 to 2018, the HEPro at PLNGS consistently measured a two-fold increase in FAC rate shortly following ion-exchange (IX) resin change-out. This will be discussed in more detail in Section 2.4.

2.1.3 CANDU-6 Reactor Design Overview

The most unique aspect of CANDU technology is the reactor core. The reactor core for both the BWR and PWR is effectively a single vertical pressure vessel, requiring the units to come completely off-line for refueling activities. In contrast, the CANDU reactor core, or calandria vessel, is orientated in a horizontal position, as shown in Figure 2.1-1. In the CANDU-6 design, the calandria vessel contains 380 fuel channels (and pressure tubes) — each fuel channel is coupled with respective inlet and outlet feeder pipes.

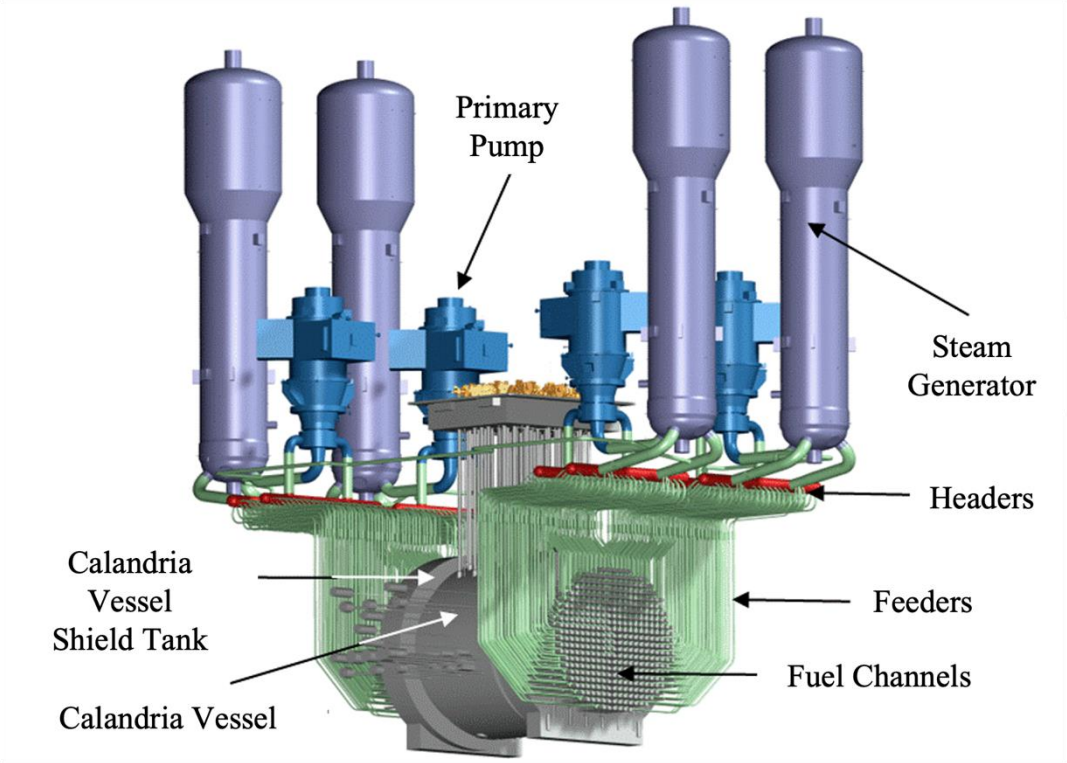

Figure 2.1-1. CANDU Reactor Configuration. [9]

Within the individual fuel channels are 12 fuel bundles. Each fuel bundle is manufactured with 37 fuel elements, each comprised of 30 natural uranium dioxide fuel pellets. The horizontal position of the calandria and the series of fuel bundles in each fuel channel allows for on-line fueling of the CANDU reactor — the use of multiple fuel bundles in series also allows for a greater degree of fuel utilization versus a single fuel bundle. The fuel bundle and fuel channels are made of zirconium alloys (Zircaloy 4 and Zr-2.5%Nb for the fuel bundle and pressure tube respectively), which contains minimal iron. Zirconium is a favorable material for reactor core components due to its high resistance to corrosion and its low neutron absorption cross-section, therefore reducing radiation build-up within the fuel channels [10].

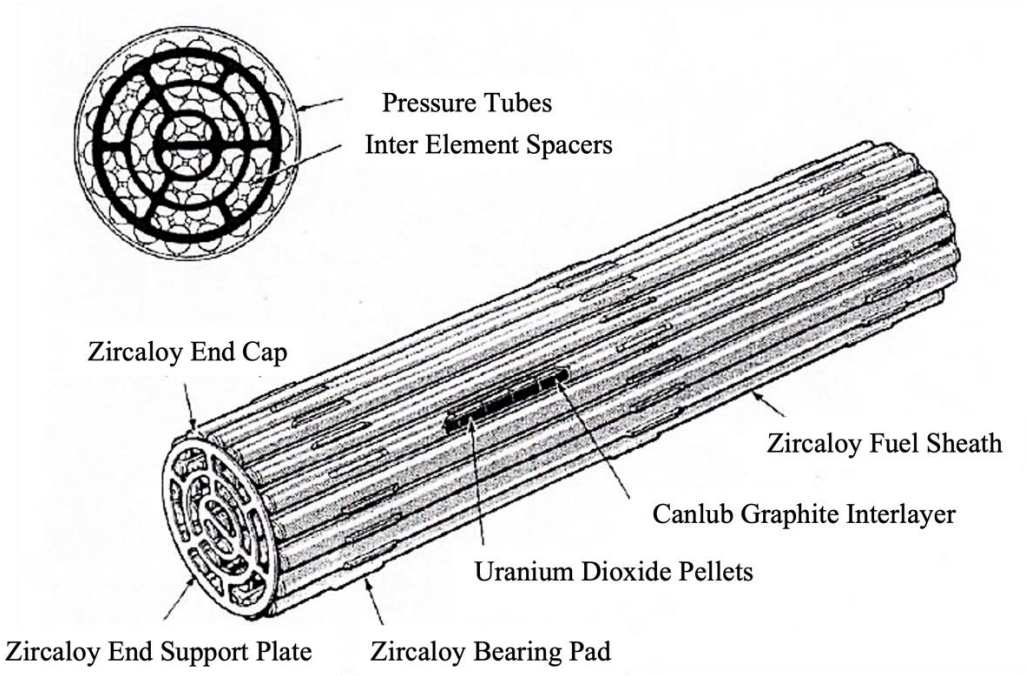

Figure 2.1-2: Pressure Tube Bundle [11]

While the majority of commercial nuclear reactor designs utilize light water exclusively, CANDU technology utilizes heavy water as both a moderator fluid and primary coolant. The neutron scattering cross-section of heavy water compared to that of light water (more than 10 times smaller) allows for natural uranium (0.7 % U-235) as a fuel source rather than enriched uranium (3-5 % U-235) needed for the PWRs and BWRs [11] [12]. Criticality is an important concept that is used to describe the state of the fission reaction. A nuclear reactor is critical when the fission process is controlled and sustainable — meaning, that of the approximate 2 to 3 neutrons released from the fission reaction, only one neutron goes on to cause another fission. Fission reactions produce neutrons travelling at extremely fast velocities. The role of the moderator is to increase the probability of a chain fission reaction by thermalizing (slowing down to "thermal" energies) the liberated neutrons, while several reactivity control devices are used to control neutron flux

and reactor power. For the CANDU, the moderator is physically separated from both the fuel and the PHTS coolant by the calandria tubes. By design, the moderator absorbs only a fraction of heat produced by the fission reaction as a result of the annuals gas between the calandria tubes and pressure tubes. The moderator is maintained at approximately 66 °C, by the cooling system briefly described in Figure 2.1-3 [13].

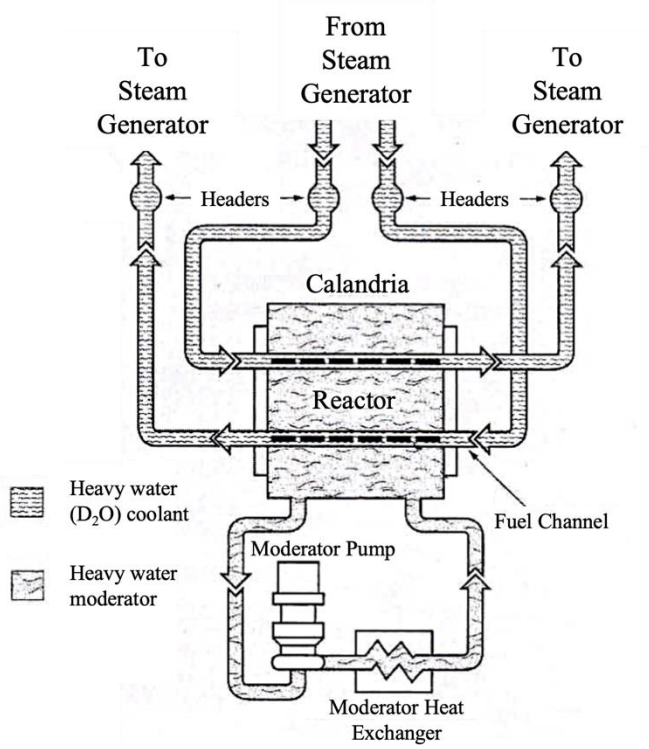

Figure 2.1-3. Primary Coolant and Moderator Fluid Circuits [13]

Heat generated by the fission reaction is transferred from the reactor core to the steam generators by the PHTS. The PHTS consists of two independent loops with coupled steam generators in a figure-of-eight pattern, as shown in Figure 2.1-4. The PHTS coolant enters the fuel channels via the inlet feeder pipes and exits via their corresponding outlet feeders. A106C carbon steel is now the standard material of construction for both the inlet

and outlet feeders, given the excessive wall thinning of the outlet feeders associated with A106B, as discussed in Section 2.1.2.

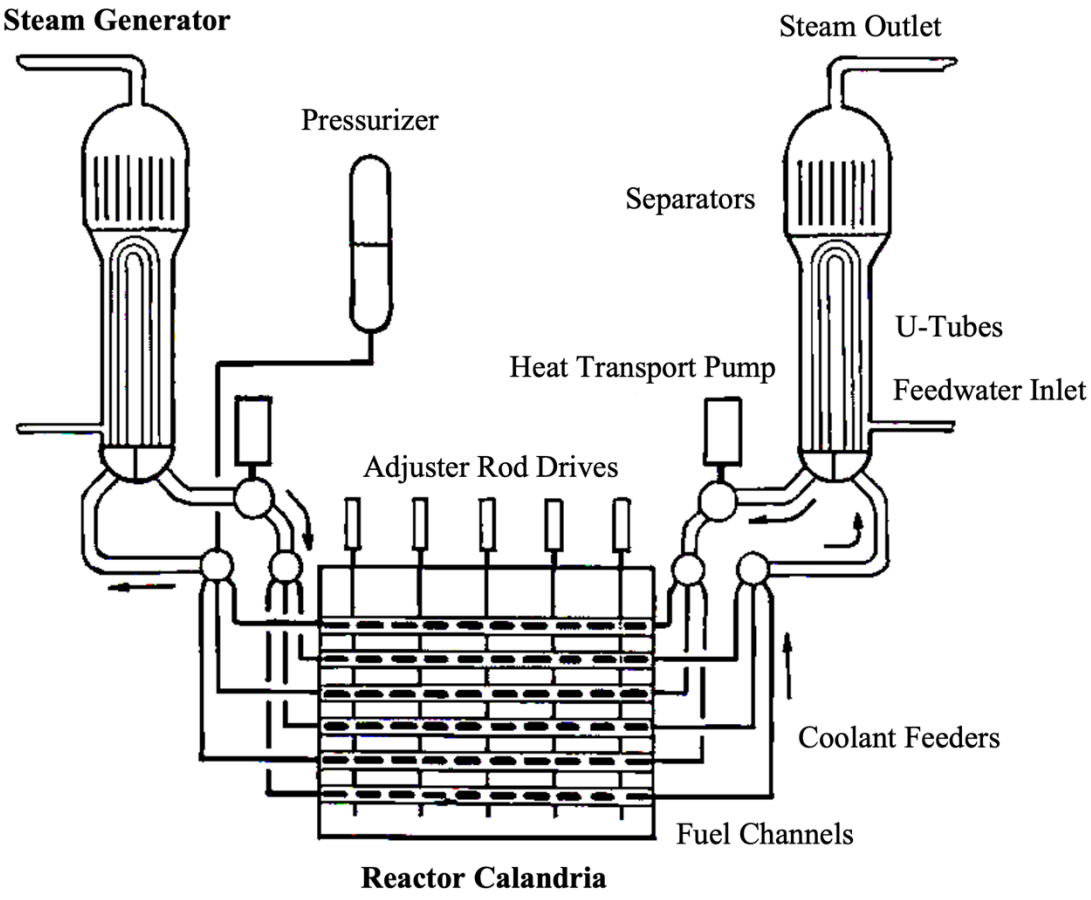

Figure 2.1-4: Simplified PHTS [14]

A $pH_{a,25°C}$[3] is maintained in the range of 10.2 to 10.4 in the PHTS coolant by addition of lithium hydroxide, which is the primary chemical used for alkalinity control in CANDU reactors. The PHTS is also injected with hydrogen gas to suppress the

[3] pH_a accounts for the natural offset of measuring the pH of heavy water using light water instruments (see Section 2.2.2).

concentration of dissolved oxygen in the coolant and prevent the radiolysis of heavy-water that may lead to corrosive environments and degradation of the purification system ion-exchange resin [10]. Table 2.1-2 summarizes the design and operational parameters of the CANDU reactor.

Table 2.1-2: Select Operating and Design Parameters for the CANDU-6 Reactor [10] [14]

Target Operating Parameters in the PHTS		Design Parameters	
Coolant flow rate	7.6 Mg/s	Moderator	D_2O
Design pressure	10.2 MPa	Coolant	D_2O
Coolant inlet temperature	260 °C	Fuel	UO_2
Coolant outlet temperature	310 °C	Fuel channels	380
$pH_{a,\ 25\ °C}$	10.2-10.4	Fuel bundles per channel	12
$[Li^+]$	0.35 - 0.55 mg/kg	Elements per bundle	37
$[D_2]$	3 - 10 mL/kg	Coolant loops	2
Dissolved O_2	< 0.01 mg/kg	Steam generators per coolant loop	2
		Heat transfer pumps per loop	2

2.1.4 PHTS Purification System

2.1.4.1 IX Resin Review

IX resins are long polymer chains with functional groups that serve as exchange sites to remove ionic impurities from fluid systems. IX resins are grouped into one of four categories: strong acid; weak acid; strong base; and weak base. The designation as either "strong" and "weak" refers to the Arrhenius definition of acids and bases, where strength is simply a measure of the degree of dissociation of H^+ or OH^-, respectively.

In the case of the CANDU PHTS purification system, strong acid and strong base resins are used because of good exchange with cations— the polymer structure for both resin types are gel polystyrene crosslinked with divinylbenzene. The strong acid resin has

sulphonic acid functional groups, as shown in Figure 2.1-5., while the strong base has type 1 quaternary ammonium functional groups [15].

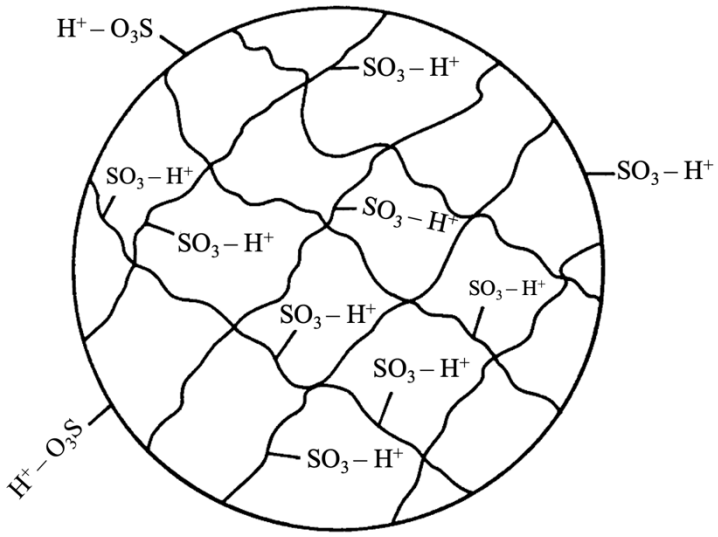

Figure 2.1-5. Schematic of Cationic Exchange Resin with Sulphonic Acid Functional Group. [16]

Eq. 2.1-1 describes the interaction between the exchange-ion on the functional group (A) and the counter-ion (B), where n is the charge of the counter-ion and R is the resin functional group.

$$nRA + B^{n+/-} \leftrightarrow (nR)B + nA^{+/-} \quad \text{Eq. 2.1-1}$$

Important properties to consider when selecting IX resin for a given process include: the stability of the resin in the given process conditions; kinetics of the exchange

reactions; swelling;[4] selectivity;[5] and total capacity[6] [16]. Table 2.1-3. gives the relative swelling and molar selectivity for various ions.

Table 2.1-3. Relative Swelling and Selectivity for Various Ionic Species.

Swelling [16]	
Monovalent ions	$Li^+ > Na^+ > K^+ > Cs^+ > Ag^+$
Polyvalent ions	Monovalent ions > $Ca^{2+} > Al^{3+}$
Selectivity [10]	
Strong Acid Resin	$Fe^{3+} > Ni^{2+} > Cu^{2+} > Fe^{2+} > Li^+ > H^+$ [17]
Strong Base (Type 1) Resin	$SO_4^{2-} > Cl^- > CHOO^- > F^- > OH^-$

The selectivity of an ion is dependent on both the ion's concentration in the resin and in the liquid solution, where the selectivity of the exchange-ion to the counter-ion is expressed as the selectivity coefficient $\left(K_{\frac{B}{A}}\right)$. Despite the affinity of one ionic species over another, the uptake of a given ionic species is also largely governed by equilibrium within the IX column [18].

$$K_{\frac{B}{A}} = {K_B}/{K_A} \qquad \text{Eq. 2.1-2}$$

$$K_{\frac{B}{A}} = \frac{c_A\, q_{BR}}{c_B\, q_{AR}} \qquad \text{Eq. 2.1-3}$$

Where:

c_A is the concentration of the exchange-ion in the liquid $\left(\frac{mol}{kg\ D_2O}\right)$

c_B is the concentration of the counter-ion in the liquid $\left(\frac{mol}{kg\ D_2O}\right)$

[4] Swelling is where the resin volume changes according to the degree of hydration.

[5] Selectivity is the affinity of the functional group towards a given ionic species.

[6] Total capacity is the number of ionic equivalents available per unit volume of resin.

K_A is the selectivity of the exchange-ion

K_B is the selectivity of the counter-ion

$K_{\frac{B}{A}}$ is the selectivity coefficient

q_{AR} is the concentration of the exchange-ion in the resin $\left(\frac{mol}{kg\ Resin}\right)$

q_{BR} is the concentration of the counter-ion in the resin $\left(\frac{mol}{kg\ Resin}\right)$

The total concentration in the liquid (C) and the total capacity of the IX resin (Q), are the sums of the concentration of the exchange-ion and counter-ion in the liquid and resin, respectively. Both the total capacity and the total concentration in the liquid solution must remain constant in order to maintain electroneutrality between the IX resin and the bulk fluid [18]. As the resin becomes spent, ionic impurities of lower valance will be "thrown" from exchange sites, releasing impurities back into the bulk fluid.

$$C = c_A + c_B \qquad \text{Eq. 2.1-4}$$

$$Q = q_{AR} + q_{BR} \qquad \text{Eq. 2.1-5}$$

Where:

C is the total concentration in the liquid $\left(\frac{mol}{kg\ D_2O}\right)$

Q is the total capacity of the IX resin $\left(\frac{mol}{kg\ Resin}\right)$

2.1.4.2 Purification System Overview

Purification auxiliary systems are integrated via "feed-and-bleed" in many CANDU processes, as maintaining proper water purity is essential for optimal unit health and performance. In addition, the PHTS purification system also serves as a the primary means of maintaining radiation fields as low as reasonably achievable (ALARA) within and around the PHTS. The PHTS purification system removes particulate and ionic impurities, such as dissolved corrosion products that have potential to become activated in

the reactor core and deposit elsewhere in the system, as well as soluble fission products that may be present in the system due to fuel failures. The purification system includes a series of heat exchangers, filters and IX columns (Figure 2.1-6). The stream of primary coolant to the purification system is cooled to ~ 60 ˚C to prevent degradation of the IX resin. The filter removes both suspended and ionic impurities that precipitate out of solution as the fluid temperature decreases (see Section 2.3), while the IX resin removes any remaining aqueous ionic impurities [10].

The PHTS purification system is configured with two types of mixed resin beds: a lithiated mixed bed (Purolite - NRW37 LiLC[7]) to remove soluble impurities; and a hydrogenated strong acid, strong base mixed bed (Dow IRN-160) that is dedicated to pH_a reduction by lithium removal. In order to maintain isotopic content of the heavy water coolant, the resins are deuterated prior to use. Following their operating lifetime, the resins are de-deuterated to recover the heavy water content. Figure 2.1-6. gives a simplified schematic of the PLNGS PHTS purification system during normal operation [10].

[7] LiLC = Lithiated, Low Chloride

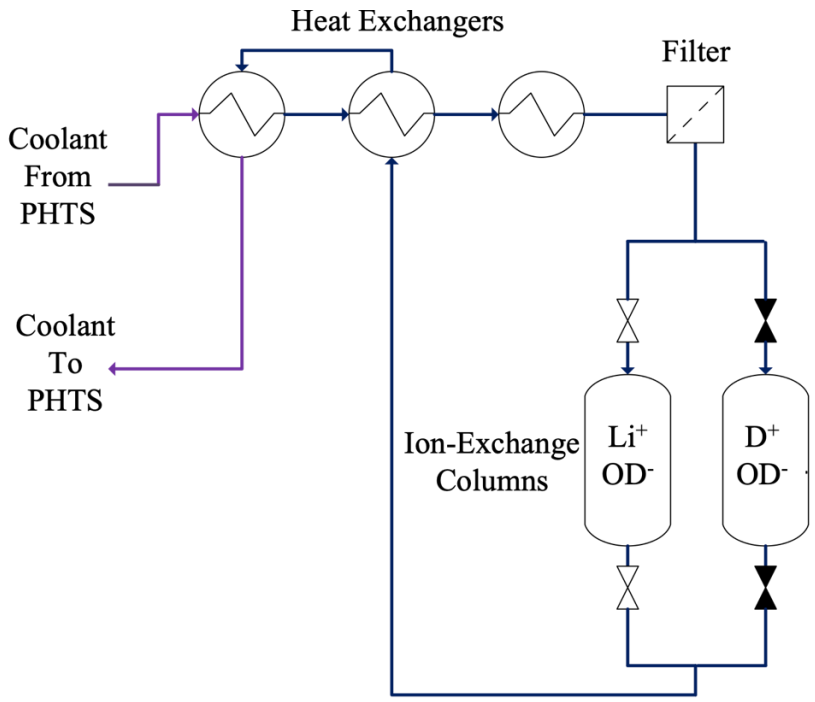

Figure 2.1-6. Simplified Schematic of PHTS Purification System. [10]

As introduced in Section 2.1.4.1, IX resins have a certain affinity towards ions with a higher valance (see Table 2.1-3.). Lithiated resin is used under normal operating conditions given that the coolant alkalinity is adjusted with lithium hydroxide; thus, the Li^+ ions will pass through the IX bed having no effect on coolant pH_a. In contrast, the deuterated column is utilized when a decrease in pH_a is necessary. The resin will exchange D^+ for Li^+ to establish an equilibrium in the deuterated column (see Section 2.1.4.1). Eq. 2.1-6 to Eq. 2.1-8 describes the exchange between the cation and anion resins and their respective ionic impurities, where Fe^{2+} and NO_3^- are used as counter-ions for lithiated and deuterated resins [10].

$$2RLi + Fe^{2+} \leftrightharpoons (2R)Fe + 2Li^+ \quad \text{Eq. 2.1-6}$$

$$2RD + Fe^{2+} \leftrightharpoons (2R)Fe + 2D^+ \quad \text{Eq. 2.1-7}$$

$$ROD + NO_3^- \leftrightharpoons RNO_3 + OD^- \quad \text{Eq. 2.1-8}$$

While all CANDU reactors have a similar fundamental design, individual stations and units have slight variations in purification system design and operating conditions — most variations are consequence of activities unique to the given reactor unit. The purification system at each CANDU station serves the same function, utilizes similar types of resin but differs in terms of purification rate[8] and anion to cation resin ratios. The IX columns are designed such that the removal of anionic impurities is prioritized, given that the only cations of significant quantity present in the primary coolant are ammonium, lithium and ferrous ions (see Section 2.4). Figure 2.1-7. gives a brief schematic of PHTS purification system configuration for all a typical CANDU-6.

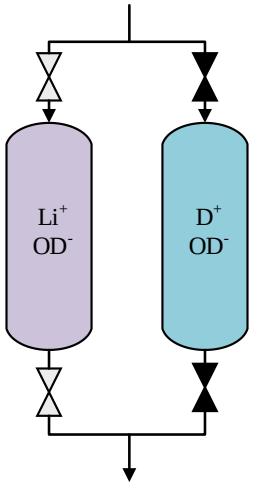

Figure 2.1-7. Schematic of Canadian CANDU-6 PHTS Purification System Configuration

[8] The purification rate varies both in terms of flow rate and percent total flow.

2.2 Corrosion and Electrochemistry

Corrosion is a process where a metal is oxidized to achieve its most thermodynamically stable state. In order for corrosion to occur, the system must have the following: anode (oxidation reaction); cathode (reduction reaction); metallic path; and an electrolyte. Consider a metal-water system, the dissolution (oxidation of the metal) produces an aqueous metal cation and a number of electrons that is equivalent to the metal's valence state. To maintain electroneutrality within the system, the oxidation reaction must *always* be accompanied by a reduction reaction to consume the released electron(s) — therefore while the oxidation and reduction reactions occur simultaneously, the reduction reaction is rate limiting [19]. For iron-water systems under reducing conditions in acidic system, the oxidation and reduction reactions are given by Eq. 2.2-1 and Eq. 2.2-2 respectively.

$$Fe_{(s)} \leftrightharpoons Fe^{2+}_{(aq)} + 2e^- \qquad \text{Eq. 2.2-1}$$

$$2H^+_{(aq)} + 2e^- \leftrightharpoons H_{2\,(g)} \qquad \text{Eq. 2.2-2}$$

If oxygen were present in the system (oxidizing conditions), the reduction reaction would become the reduction of oxygen, rather than reduction of hydrogen. The reduction reaction for oxygen under acidic and alkaline conditions are given by Eq. 2.2-3 and Eq. 2.2-4 respectively. Eq. 2.2-5 gives the hydrogen evolution reaction under alkaline conditions.

$$\tfrac{1}{2}O_{2\,(aq)} + 2H^+_{(aq)} + 2e^- \leftrightharpoons H_2O \qquad \text{Eq. 2.2-3}$$

$$\tfrac{1}{2}O_{2\,(aq)} + H_2O + 2e^- \leftrightharpoons 2OH^-_{(aq)} \qquad \text{Eq. 2.2-4}$$

$$2H_2O + 2e^- \leftrightharpoons H_2 + 2OH^- \qquad \text{Eq. 2.2-5}$$

While there are many conditions that facilitate corrosion processes, it all depends upon electrochemical mixed potential and concentration equilibria.

2.2.1 Corrosion Thermodynamics

The standard potential (E°) of an electrochemical system is dependent on the standard Gibb's Free Energy of the reaction (ΔG°_{rxn}). The standard potential assumes that the system is at standard-conditions, meaning that the metal is in contact with a solution of its own ions at unit activity, and operating 1 atm [20].

$$E^{\circ} = \frac{-\Delta G^{\circ}_{rxn}}{nF} \qquad \text{Eq. 2.2-6}$$

Where:

F is Faraday's constant $\left(96485.3 \frac{C}{mol}\right)$

n is the number of electrons transferred

As standard conditions are not typically realized in practice, the Nernst equation (Eq. 2.2-7) is used to estimate the equilibrium potential $\left(E_{eq}\right)$ of non-ideal solutions. Given that potential cannot be measured directly, standard and equilibrium potentials are referenced against the standard hydrogen electrode (SHE) [20].

$$E_{eq} = E^{\circ} + \frac{RT}{nF} ln\left(\frac{a_{oxidized}}{a_{reduced}}\right) \qquad \text{Eq. 2.2-7}$$

Where:

R is the Ideal Gas constant $\left(8.314 \frac{m^3\ Pa}{mol\ K}\right)$

T is the temperature (K)

$a_{oxidized}$ is the activity of oxidized species

$a_{reduced}$ is the activity of reduced species

2.2.1.1 Pourbaix Diagrams and Protective Oxide-Film Formation

Pourbaix diagrams consolidate the influence of temperature, pressure, concentration of the aqueous metal, and system pH, on the equilibrium potential for all possible corrosion products. A Pourbaix diagram illustrates the equilibrium potential of corrosion

products as a function of pH, essentially serving as a “map” for describing corrosive, passive and noble operating regions — thus serving as useful tools for determining if a metal is suitable for application under a given set of system conditions. Understanding what system conditions facilitate the formation of protective oxide-films is paramount to optimizing corrosion resistance in industrial processes.

Pourbaix diagrams utilize the Nernst equation (recall Eq. 2.2-7) to determine the equilibrium potential for reactions of the following nature: pure electron transfer; pure acid-base reaction, and electrochemical reactions consisting of charge transfer and acid-base reactions — which are represented by *solid* horizontal, vertical and diagonal lines on the Pourbaix diagram, respectively.

Figure 2.2-1. gives a Pourbaix diagram for an iron-water system under similar conditions experienced by the PHTS outlet feeders. Important components to note are the diagonal and vertical *dashed lines*. The diagonal lines represent the reduction reactions of oxygen and hydrogen, while the dashed vertical line represents neutral pH at the given system temperature. The area between the hydrogen and oxygen reduction lines represents the region water stability ― meaning that operating outside this region will cause an equilibrium shift, therefore evolving either hydrogen or oxygen gas, or both.

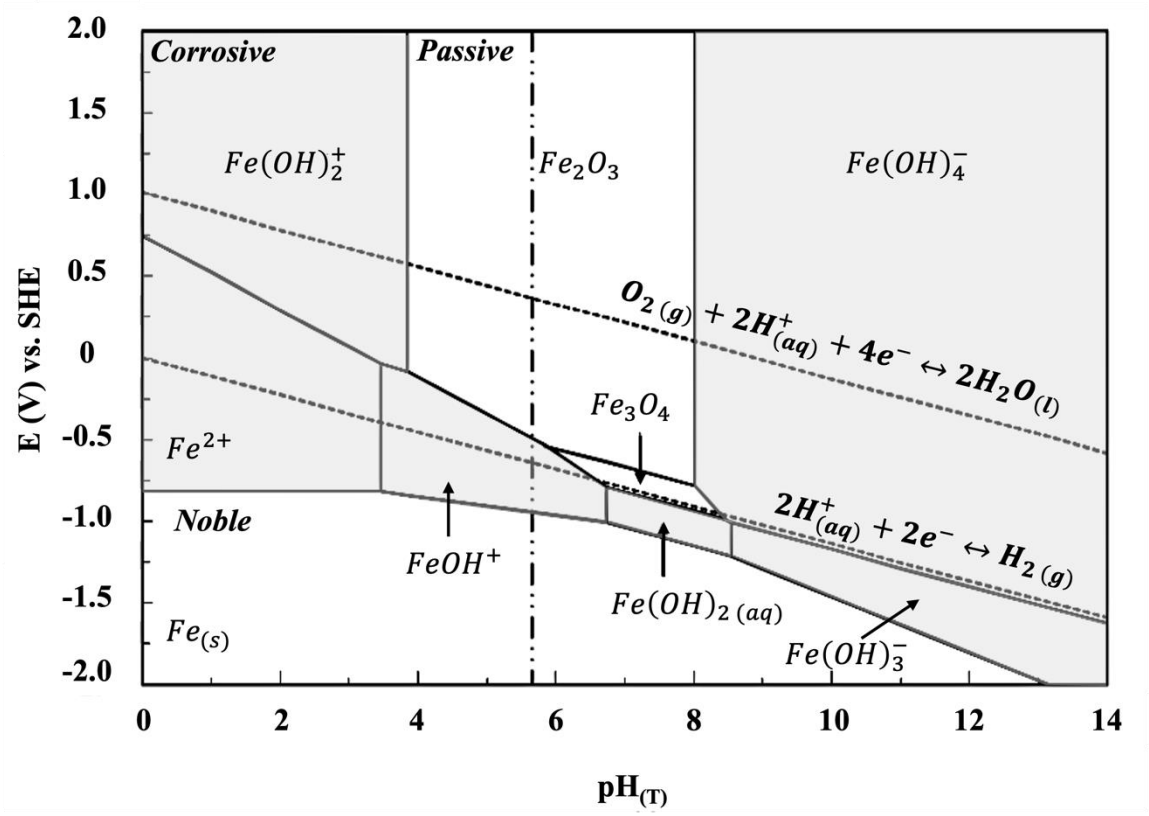

Figure 2.2-1. Pourbaix Diagram an the Iron-Water System at 300 °C, 10 MPa, and 10^{-8} mol/kg. [21]

Figure 2.2-1. gives the regions where magnetite (Fe_3O_4) and hematite (Fe_2O_3) exist at CANDU PHTS conditions [22]. Given that high concentrations of dissolved oxygen can be problematic in the CANDU PHTS, the dissolved oxygen concentration is kept low such that the reduction of hydrogen is the dominating cathodic reaction — thus, necessitating the formation of a magnetite film, as given in Eq. 2.2-8, where x represents the charge of the dominant iron hydrolysis products (see Section 2.3.2). Approximately one half of the iron (II) corrosion products forms magnetite directly at the metal-electrolyte interface, while the other half migrates to the bulk solution and is eventually hydrolyzed as shown in Eq 2.2-8 [23].

$$3Fe(OH)_x^{2-x} + (4-3x)H_2O \leftrightarrow Fe_3O_4 + (6-3x)H^+ + H_2 \qquad \text{Eq. 2.2-8}$$

2.2.2 Conductivity and pH

Controlling pH_a in the optimal range to promote the formation of a protective oxide-film requires a reliable means of measuring and controlling $pH_{a,\,25°C}$ of the bulk fluid. The pH of a system is defined as the concentration of hydrogen ions present, expressed on a logarithmic scale. For concentrated solutions, where the ionic strength is high, activity of the hydrogen ions is used to calculate pH, as per Eq. 2.2-9. For dilute solutions (concentrations below $10^{-3}\,\frac{mol}{kg}$ — such as in the PHTS), where the ionic strength is low, the ionic activity coefficient is at unity (1), thus allowing for the direct utilization hydrogen ion concentration, as given in Eq. 2.2-11 [10].

$$pH = -log_{10}(a_{H^+}) \qquad \text{Eq. 2.2-9}$$

$$a_{H^+} = \gamma_{\pm}\frac{m_{H^+}}{m^o} \qquad \text{Eq. 2.2-10}$$

$$pH = -log_{10}([H^+]) \qquad \text{Eq. 2.2-11}$$

Where:

a_{H^+}	is the activity of the hydrogen ions in the solution
m_{H^+}	is the concentration of the hydrogen ions $\left(\frac{mol}{kg}\right)$
m^o	is the activity of the standard reference state $\left(1\,\frac{mol}{kg}\right)$
$\gamma_{\pm}$	is the ionic activity coefficient
$[H^+]$	is the concentration of hydrogen ions in the solution $\left(\frac{mol}{kg}\right)$

The same method can be applied to heavy water systems to determine pD (where "D" is deuterium) if the concentration of deuterium ions in the solution is known. Unfortunately, pD cannot be measured directly given that pH electrodes are designed and calibrated with the intended use in light water systems. Instead, it is standard to correct readings of an alkaline heavy water solution to an apparent pH (pH_a) value, as shown in Eq. 2.2-12 [10].

$$pH_a = pH + 0.456 \qquad \text{Eq. 2.2-12}$$

As briefly noted in Section 2.1.3, pH_a accounts for the natural offset of measuring the pH of heavy water using light water instruments, due to the less dissociative nature of heavy water compared to light water at equal conditions[9]. Both light water and heavy water will dissociate into their ionic dissociation products, as given by Eq. 2.2-13 and Eq. 2.2-14, respectively. The concentration of the dissociation products is dependent on the dissociation constant of water, which varies based on both temperature and the presents of other ionic species in the bulk fluid [10].

$$H_2O \rightleftharpoons H^+ + OH^- \qquad \text{Eq. 2.2-13}$$

$$D_2O \rightleftharpoons D^+ + OD^- \qquad \text{Eq. 2.2-14}$$

The dissociation constant of water is expressed as the ratio of the product of the activity of each dissociation product to the activity of water, where at dilute conditions the activity of water is unity (1). As with the pH discussion above, activity can be taken directly as concentration for pure or dilute solutions [10].

[9] $K_{w(heavy),25℃} = 1.35 \times 10^{-15}$

$$K_w = \frac{[H^+][OH^-]}{[H_2O]} \qquad \text{Eq. 2.2-15}$$

Where:

K_w	is the dissociation constant of water
$[OH^-]$	is the concentration of the hydroxide ions $\left(\frac{mol}{kg}\right)$
$[H_2O]$	is the concentration of water $\left(\frac{mol}{kg}\right)$

At neutral conditions in pure light water ($pH_{25°C} = 7$), the concentration of hydrogen ions and hydroxide ions are equal. Rearranging Eq. 2.2-11, and solving for Eq. 2.2-15, respectively, gives the following [10]:

$$[H^+] = 10^{-pH} = 10^{-7} = 10^{-7}\frac{mol}{L}$$

$$\therefore \quad [OH^-] = 10^{-7}\ \frac{mol}{L}$$

$$\therefore \quad K_{w(light),25°C} = \ 10^{-14}$$

Should another ionic species be introduced into the system, the dissociation of water into its respective ionic species will shift to maintain charge neutrality of the bulk solution, thus shifting pH. In the case of the PHTS, lithium hydroxide is added to the bulk fluid to achieve the desired operating $pH_{a,\,25°C}$ of 10.2 ($pH_{25°C} = 9.8$). Since lithium hydroxide is a strong base, it is effectively completely dissociated at PHTS conditions as per Eq. 2.2-16 [10].

$$LiOH \rightleftharpoons \ Li^+ + OH^- \qquad \text{Eq. 2.2-16}$$

From the dissociated equation given above for lithium hydroxide, the concentration of lithium required to shift the $pH_{25°C}$ in the PHTS to 9.8 is equal to the concentration of hydroxide ions in the bulk solution, and therefore is easily determined by using Eq. 2.2-11 and Eq. 2.2-15

$$[H^+] = 10^{-9.8} = 1.59 \times 10^{-10} \frac{mol}{L}$$

$$[OH^-] = \frac{10^{-14}}{1.58 \times 10^{-10}} = 6.31 \times 10^{-5} \frac{mol}{L}$$

$$\therefore \quad [Li^+] = 6.31 \times 10^{-5} \ \frac{mol}{L}$$

As with electrical cables, electrical energy migrates in solutions via potential gradients. The conductivity of a solution is dependent on both the concentration and speciation of the charge carrying-ions. Molar conductivity of a solution is essentially the ratio of the total specific conductance of the solution to its stoichiometric molar concentration [10].

$$\Lambda_m = \frac{k}{c} \qquad \text{Eq. 2.2-17}$$

Where:

Λ_m is the molar conductivity $\left(\frac{S\ cm^2}{mol\ eq}\right)$

k is the specific conductance of the solution $\left(\frac{S}{m}\right)$

c is the stoichiometric molar concentration of the solution

For infinitely dilute solutions, the contribution of a given ion species can be measured if the concentrations of the ionic species are known. In this case, the known specific conductance of the electrolyte can be taken as the summation of specific conductance of the ion species present, where the specific conductance of the ions is the product of the molar conductivity of the ion and its concentration in the solution. Molar conductivities for ions at infinite dilution are tabulated and readily available in various literatures. Table 2.2-1 gives values of cations and anions relevant to this discussion [10].

$$k = \sum_i k_i \qquad \text{Eq 2.2-1}$$

$$k_i = \lambda_{m,i} c_i \qquad \text{Eq 2.2-2}$$

Where:

k_i	is specific conductance of the ion $\left(\frac{S}{cm}\right)$
c_i	concentration of the ion $\left(\frac{mol}{cm^3}\right)$
$\lambda_{m,i}$	molar conductivity on the ion $\left(\frac{S\ cm^2}{mol\ eq}\right)$

Table 2.2-1. Molar Conductivities of Ions at Infinite Dilution [10]

Cations $\left(\frac{S\ cm^2}{mol\ eq}\right)$		Anions $\left(\frac{S\ cm^2}{mol\ eq}\right)$	
H^+	349.7	OH^-	198
D^+	249.9	OD^-	119
Li^+	38.7		

Combining the concepts given above into a nomogram creates a valuable tool for CANDU stations to accurately validate and adjust bulk fluid pH_a, thus maintaining optimal health and longevity of PHTS systems. The bulk pH_a is calculated from the lithium concentration, which is determined using an in-situ conductivity meter. Periodically ion chromatography is performed on grab samples to validate lithium concentrations (and associated pH_a). Figure 2.1-1 gives a nomogram constructed specifically to correlate the lithium

concentration, conductivity and pH_a at 25°C in the PHTS[10]. Line "A" represents a correlation where pH_a is the known variable. Line "B" represents a correlation where contamination in the PHTS is present. Line "C" gives the actual equivalent high temperature alkalinity expressed as pH_a [24].

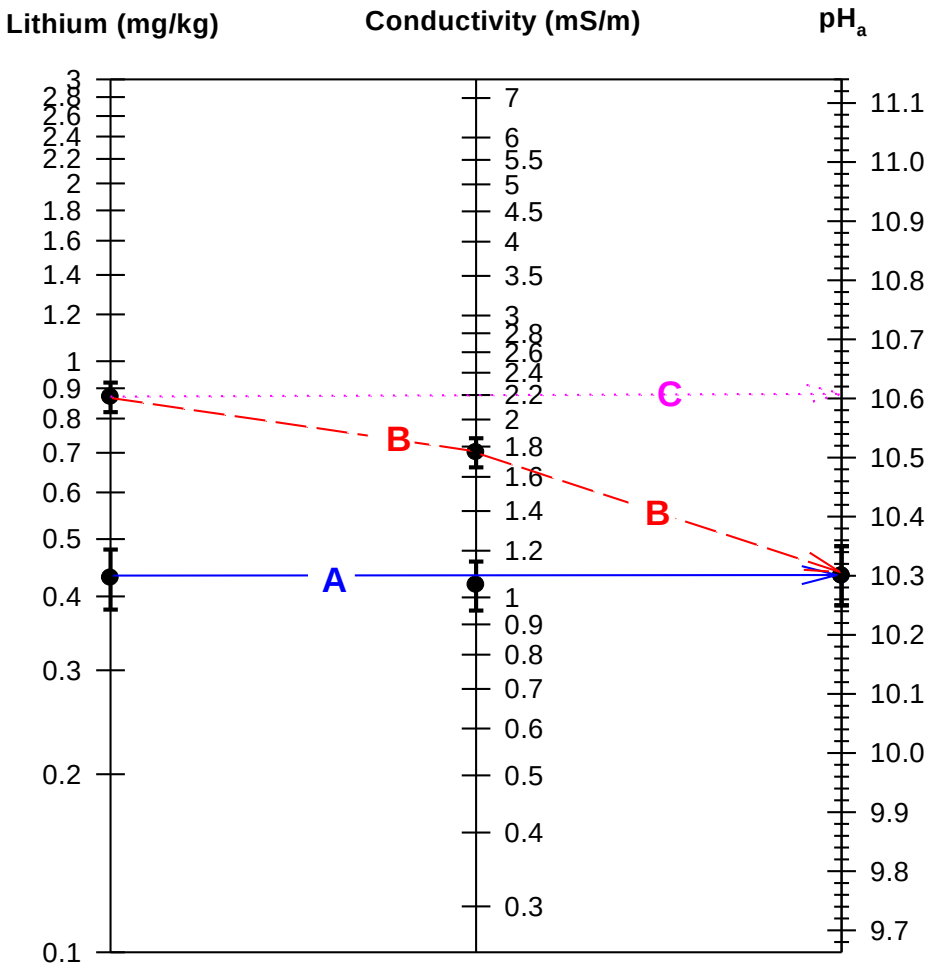

Figure 2.2-2. Correlation PHTS Data for Lithium Concentration, Conductivity and pH_a at 25°C [25]

[10] To use the nomogram only one known variable is required. The remaining two variables are determined by drawing a straight line that intersects their respective scales, where the values are taken at the intersection.

2.2.3 Corrosion Kinetics

Thermodynamics is the study of energy within a system — meaning that while thermodynamics provide valuable insight to possible corrosion mechanisms and products, it does not provide details describing the rate at which corrosion processes occur. Understanding the rate, or kinetics, of corrosion processes goes hand-in-hand with the importance of understanding what conditions facilitate the formation of protective oxide-films (see Section 2.3).

The rate at which corrosion processes occur is described by the rate of electron transfer from the anodic reaction to the cathodic reaction. Given that the coupled redox reactions occur simultaneously, the rate at which the anodic reaction releases electrons (i_a) is both equal and opposite of the rate at which the electrons are consumed by cathodic reaction (i_c) — which is known as the exchange current density or the corrosion current (i_o).

$$i_o = i_a = -i_c \qquad \text{Eq. 2.2-18}$$

From the previous section we know that every stable species exists at an equilibrium potential. Corrosion occurs when the actual potential (E_{act}) of a given species is removed from its equilibrium potential (E_{eq}), therefore making it unstable — the degree at which the species is removed from its equilibrium potential is known as overpotential (η).

$$\eta = E_{act} - E_{eq} \qquad \text{Eq. 2.2-19}$$

The Butler-Volmer equation describes current (i) as a function of overpotential for a *single redox reaction*, which consists of two competing (anodic and cathodic) exponential terms. The symmetry coefficient (β) can influence the reaction kinetics depending on the rates at which the forward and reverse reactions occur. The symmetry coefficient is

determined experimentally for a given system, however, assuming a symmetry coefficient of 0.5 is usually a good approximation [25].

$$i = i_o \left\{ exp\left[\frac{(1-\beta)nF}{RT}\eta\right] - exp\left[\frac{\beta nF}{RT}\eta\right]\right\} \qquad \text{Eq. 2.2-20}$$

For a redox reaction, the anodic reaction will occur at a higher potential than the equilibrium potential, while the cathodic reaction will occur at a potential lower than the equilibrium potential, therefore, the Butler-Volmer equation can be broken into anodic and cathodic terms, as given by Eq. 2.2-21 & Eq. 2.2-22, respectively. Either the anodic or the cathodic reaction will dominate the overall *single redox reaction*, meaning that for a *coupled redox reaction*, the cathodic term in the oxidation reaction and the anodic term in the reduction reaction can both be neglected.

$$i = i_a = i_o exp\left[\frac{(1-\beta)nF}{RT}\eta_a\right] \qquad \text{Eq. 2.2-21}$$

$$i = i_c = -i_o exp\left[-\frac{\beta nF}{RT}\eta_c\right] \qquad \text{Eq. 2.2-22}$$

For a coupled redox reaction the corrosion current can be determined graphically using an Evans Diagram. An Evans Diagram plots potential as a function of $\log_{10}$ of the absolute current, where the corrosion current is the point at which the potential for the coupled redox reactions intersects, as illustrated in Figure 2.2-3. Evans Diagrams are also useful for determining the limiting current (i_{lm}), which describes the point where mass transfer, rather than potential, drives the reaction rate for the corrosion process.

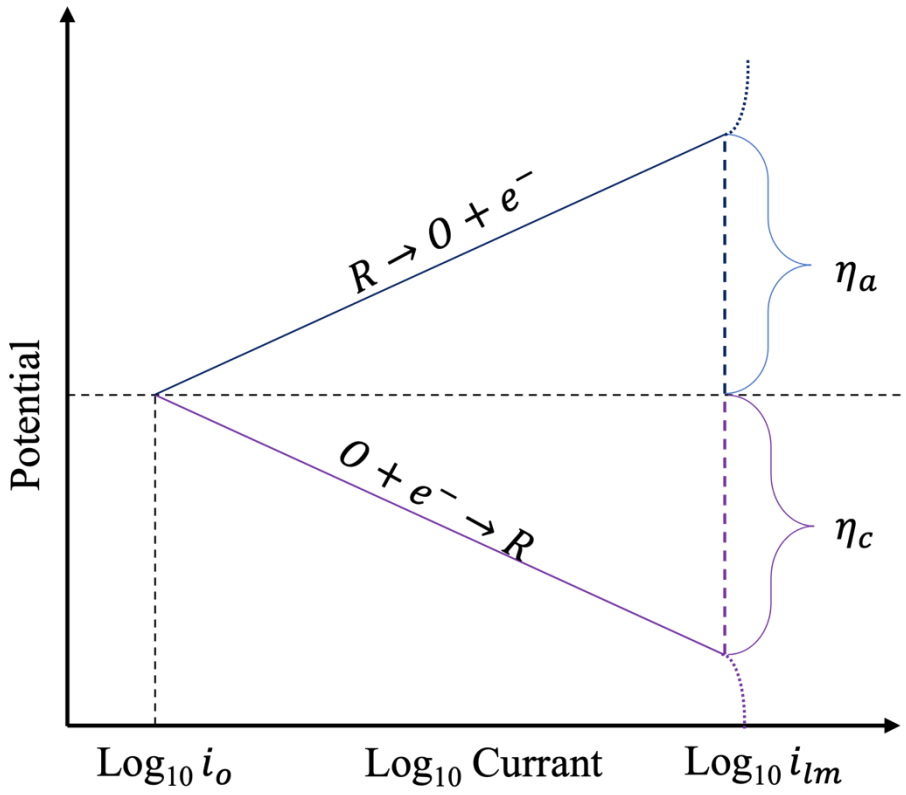

Figure 2.2-3. Evans Diagram for a single redox reaction.

2.3 Magnetite Formation and Solubility

The concepts covered in Section 2.2 indicate that the electrochemical characteristics of corrosion processes are highly dependent on the concentration of the corroding metal in the system. Understanding how operating conditions influence the formation and solubility of magnetite are paramount to understanding the FAC mechanism and how to mitigate it. The two predominant studies of magnetite solubility were performed by Sweeton and Baes in 1970 and Tremaine and Leblanc in 1980 [3] [26]. The solubilities reported by both parties agree in terms of trend behaviour, however, the solubility data reported by Tremaine and Leblanc are lower than what was reported by Sweeton and Baes by

approximately an order of magnitude in the pH range of approximately 8 to 12. The solubility data is given in Figure 2.3-1.

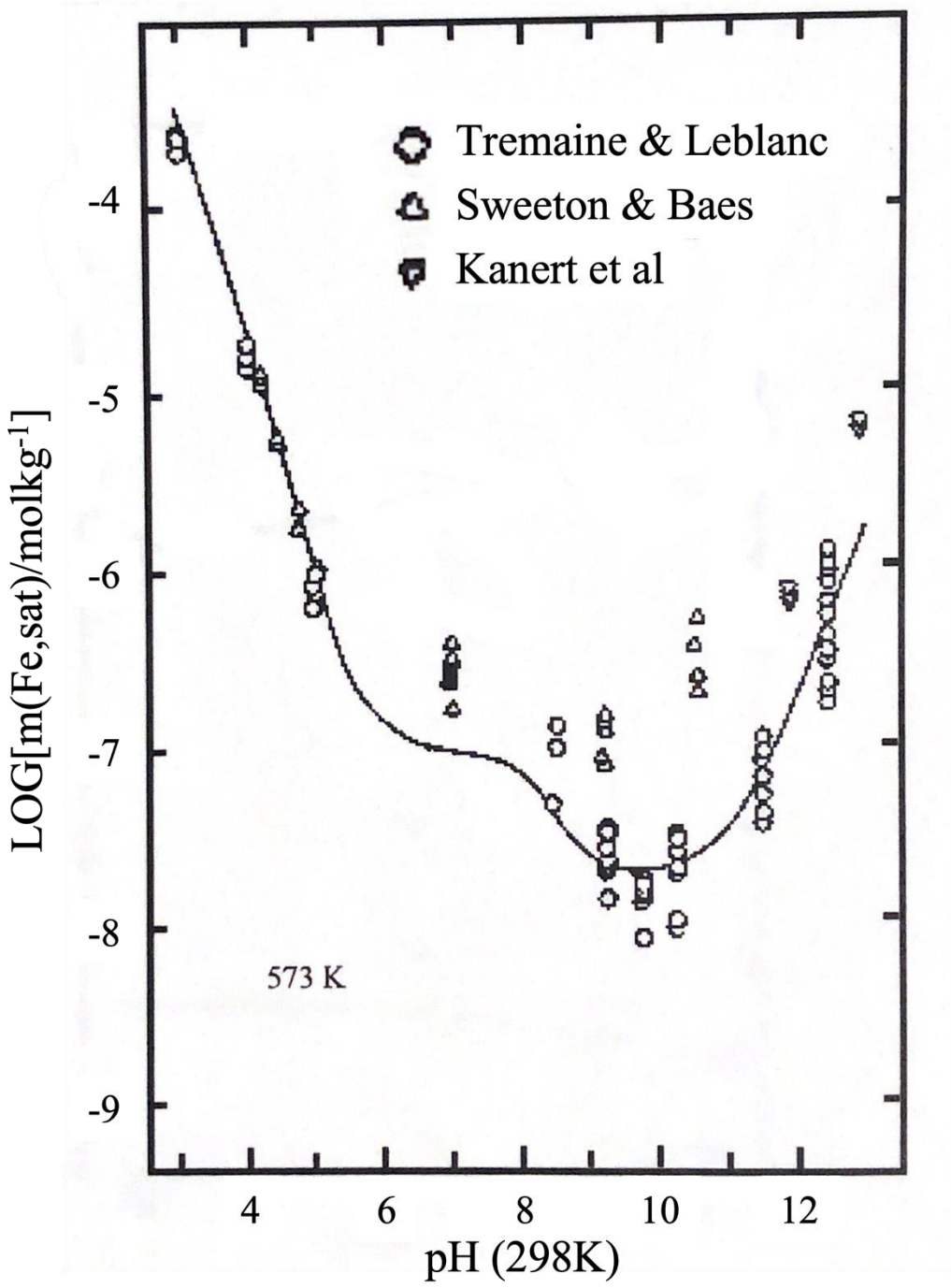

Figure 2.3-1. Comparison of Tremaine and Leblanc Magnetite Solubility Data Versus Sweeton and Baes. [3] [26] [27]

2.3.1 Formation of Magnetite Films

As discussed in Section 2.2.1.1, magnetite formation at CANDU PHTS conditions can only occur over a particular pH_a range. Magnetite's range of formation is due to its solubility dependance on pH_a (see Section 2.3.2). In the early stages of corrosion, a corroding metal will experience high rates of metal dissolution, which decreases over time as the concentration of the metal in the bulk fluid increases and oxide films form on the metal surface. Oxide-films are formed once the solubility limit of the corroding metal is reached, thus, causing the metal to precipate from solution. The magnetite films formed in the inet feeder pipes of CANDU reactors are of the Potter-Mann type, which are characterised by their inner and outer oxide layers – a double layer, as illustrated in Figure 2.3-2. The magnetite films formed in the inlet feeders consist of well formed crystals [28] and have a thickness of 40-75 µm or greater [29] that accounts for both the inner and outer layers. In contrast, the area of the outlet feeder pipes that are experiencing the largest rates of FAC are only capable of forming single layer magnetite films with an approximate thickness of 1-2 µm

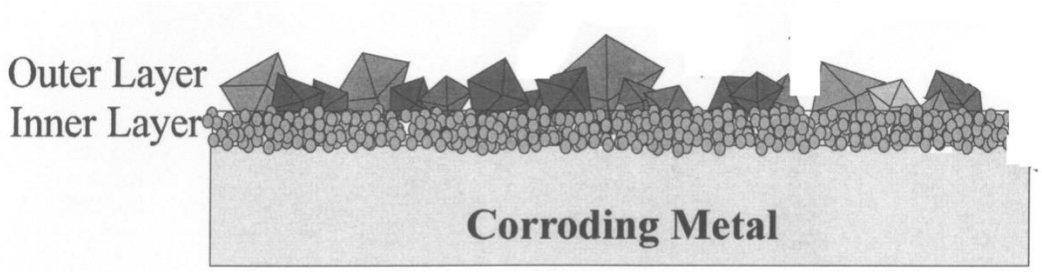

Figure 2.3-2. Cross-Section of Magnetite Formation. [30]

2.3.2 Magnetite Solubility

The difference in magnetite film thickness in the inlet and outlet feeder pipes is fundamentally due to how the solubility of magnetite varies with temperature and the bulk fluid concentration at both regions. Eq. 2.3-1 is a simplified form of the description of the rate of FAC ($\dot{m}$) as a function of the difference between the iron-saturation concentration, or total iron solubility, (C_{sat}) and the concentration of iron species in the bulk fluid (C_b), where k is a kinetic constant[11] [2].

$$\dot{m} = k(C_{sat} - C_b) \qquad \text{Eq. 2.3-1}$$

Figure 2.3-3 demonstrates how the total solubility of iron varies as a function of temperature for a number of pH values. Operating at a pH of 9.8 ($pH_{a,\,25^{\circ}C}$ of ~ 10.2) gives the lowest difference iron solubility between the outlet and inlet feeder pipe temperatures (310 ˚C and 260 ˚C, respectively). Given that the difference between the iron solubility and the concentration of iron in the bulk fluid is a primary driving force for FAC, it is important that the system is operated at a pH_a that achieves the lowest iron solubility at both inlet and outlet feeder conditions. Furthermore, pH selection must provide sufficient operating margin above the 9.0 – 9.4 pH range, at which the solubility of iron varies inversely with the increasing coolant temperature along the reactor core. Adequate solubility prevents iron deposition in the core that would be subject to activation by neutron bombardment, thus facilitating ALARA radiation fields in both in the PHTS coolant and ex-core.

[11] k may be taken as the mass transport coefficient and has an estimated value of 0.01 m/s; however, it is actually a combined constant incorporating both mass transfer and dissolution kinetics of the magnetite film.

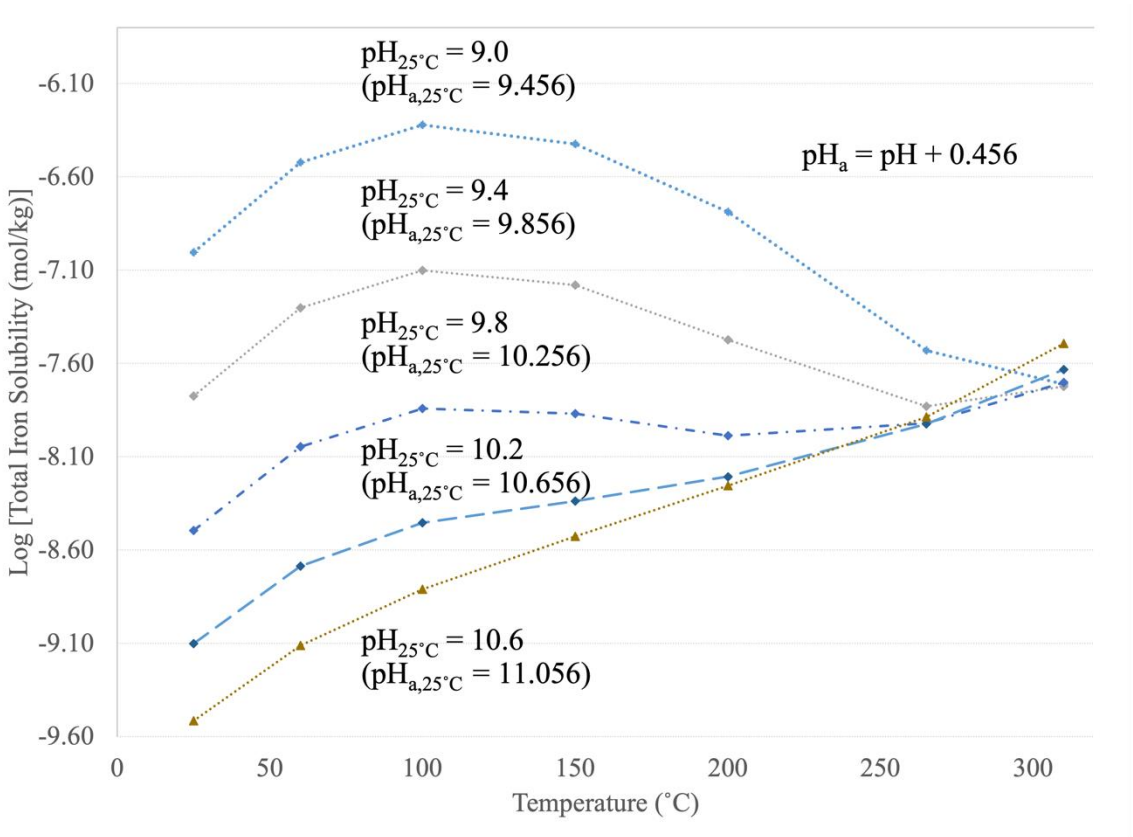

Figure 2.3-3: Total Iron Solubility as a Function of Temperature in Light Water [3]

Figure 2.3-4 also illustrates how iron solubility varies at different locations within the CANDU PHTS and purification system. The temperature of the primary bulk fluid decreases from 310 ˚C to ~ 260 ˚C when progressing through the steam generators. The decrease in temperature results in a decrease of iron solubility in all cases considered (except for pH of 9.0), which causes ferrous oxides to precipitate and form a protective double oxide layer in the steam generators and inlet feeder pipes — *therefore protecting the inlet feeders from FAC*. The primary bulk fluid passes through the reactor core where it is once again heated to 310 ˚C. The absence of iron in the reactor core and the significant amount of iron precipitated in the inlet feeders results in an undersaturated solution and significant iron (magnetite) dissolution between the fuel channel and the outlet feeder coupling [10].

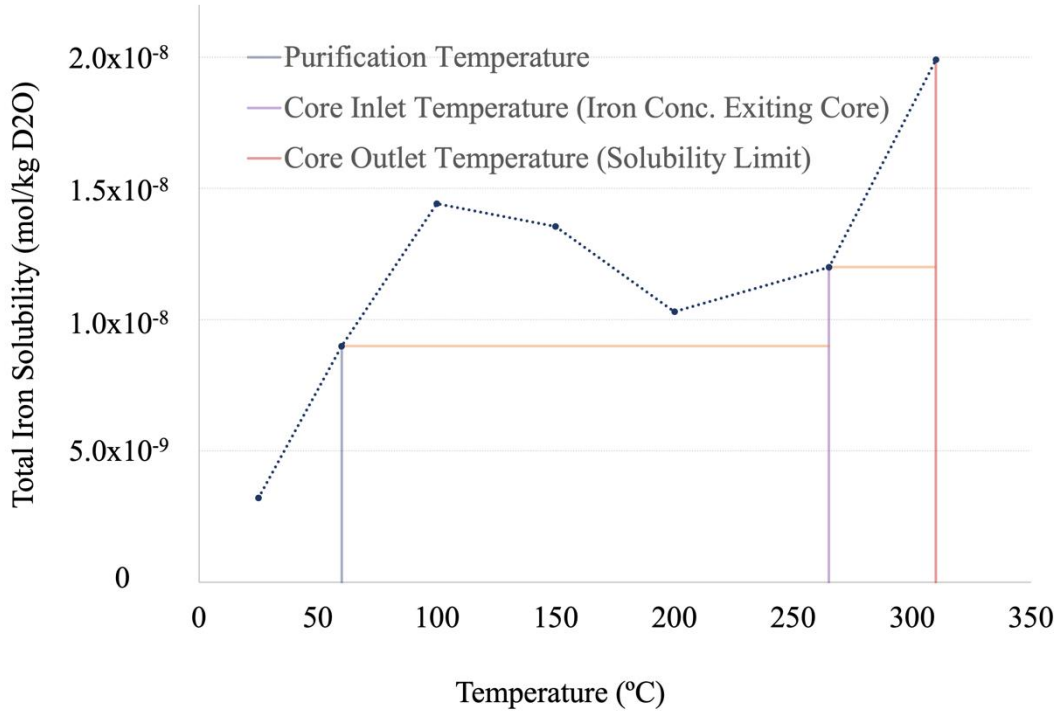

Figure 2.3-4. Total Solubility of Iron in Heavy Water at a $pH_{a,\,25^{\circ}C}$ of 10.2 ($pH_{25^{\circ}C}$ of 9.8) [3]

Figure 2.3-5 shows the distribution of iron hydrolysis species and total iron solubility as a function of pH at 310 ˚C [3]. Approximately one-half of the iron ions produced migrate to the bulk solution where they become hydrolyzed to form the dominant iron oxide products described by Eq. 2.3-2 and Eq. 2.3-3, while the other half is incorporated in the oxide film [6].

$$Fe^{2+} + 2OH^{-} \leftrightharpoons Fe(OH)_2 \qquad \text{Eq. 2.3-2}$$

$$Fe^{3+} + 3OH^{-} \leftrightharpoons Fe(OH)_3 \qquad \text{Eq. 2.3-3}$$

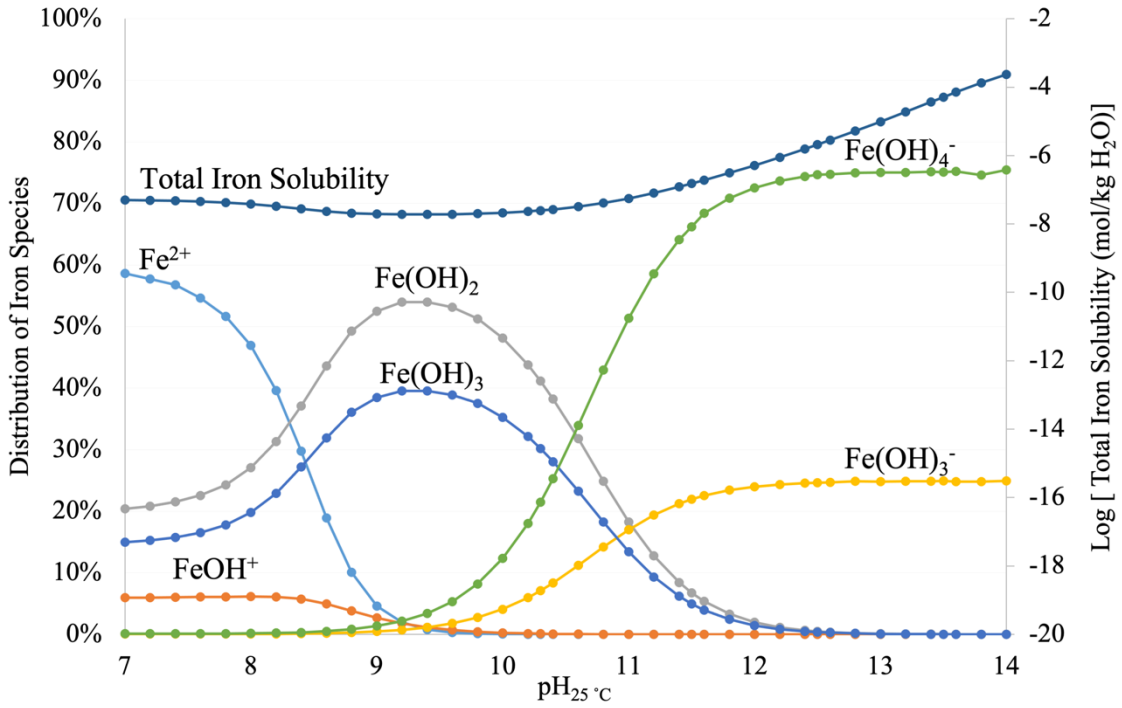

Figure 2.3-5 Total Iron Solubility and Species Composition at 310 ˚C. [3]

2.4 Observed FAC Rate Increase Following IX Resin Change-Out

As described in Section 2.1.2, since 2016 the HEPro at PLNGS has consistently reported a two-fold increase in FAC rate shortly following an approximately yearly IX resin change-out. Pertinent data gathered pre- and/or post-IX resin change-out from years 2016 to 2018 are illustrated in Figure 2.4-1 to Figure 2.4-3, respectively. The figures illustrate: derived FAC rate from the HEPro; bulk pH_a/lithium concentration and ammonia concentration. The bulk pH_a and lithium concentrations are inferred by an in-situ conductivity meter and correlations. The bulk pH_a is calculated from the measured lithium concentration and pH_a and lithium concentration results are verified periodically by grab samples. The ammonium ion concentration, which is produced in the reactor via radiolysis of dissolved nitrogen, is measured by grab sample only.

Figure 2.4-1 shows the data collected from the HEPro operation between February 2016 to April 2016, where the reactor was shut down for an annual maintenance outage. Figure 2.4-1 shows an increase in hydrogen gas production rate (and derived FAC rate – see Eq. 3.3-4) immediately following IX resin change-out, with a more significant increase in the days to follow as readily seen in the increased "pumpdown" frequency on the pink line. The FAC rate increased slightly from approximately 15-20 µm/a to 25 µm/a while the ammonium concentration is decreasing, then increases significantly to 40-45 µm/a once the ammonium ions are completely removed from the bulk fluid (or below the detection limit). As the ammonium builds in the bulk fluid, the FAC rate decreases and holds around 30 µm/a until the unit is shut down.

In 2017 the IX resin was replaced *following* the annual maintenance outage. Unfortunately, the HEPro was out of service shortly before and for about week or so following the IX resin replacement due to a power failure in the HEPro system. In 2018 the IX resin was replaced *during* the annual planned maintenance outage. The chemistry trends from 2017 and 2018, Figure 2.4-2 and Figure 2.4-3, respectively, ultimately agree with the data observed from 2016.

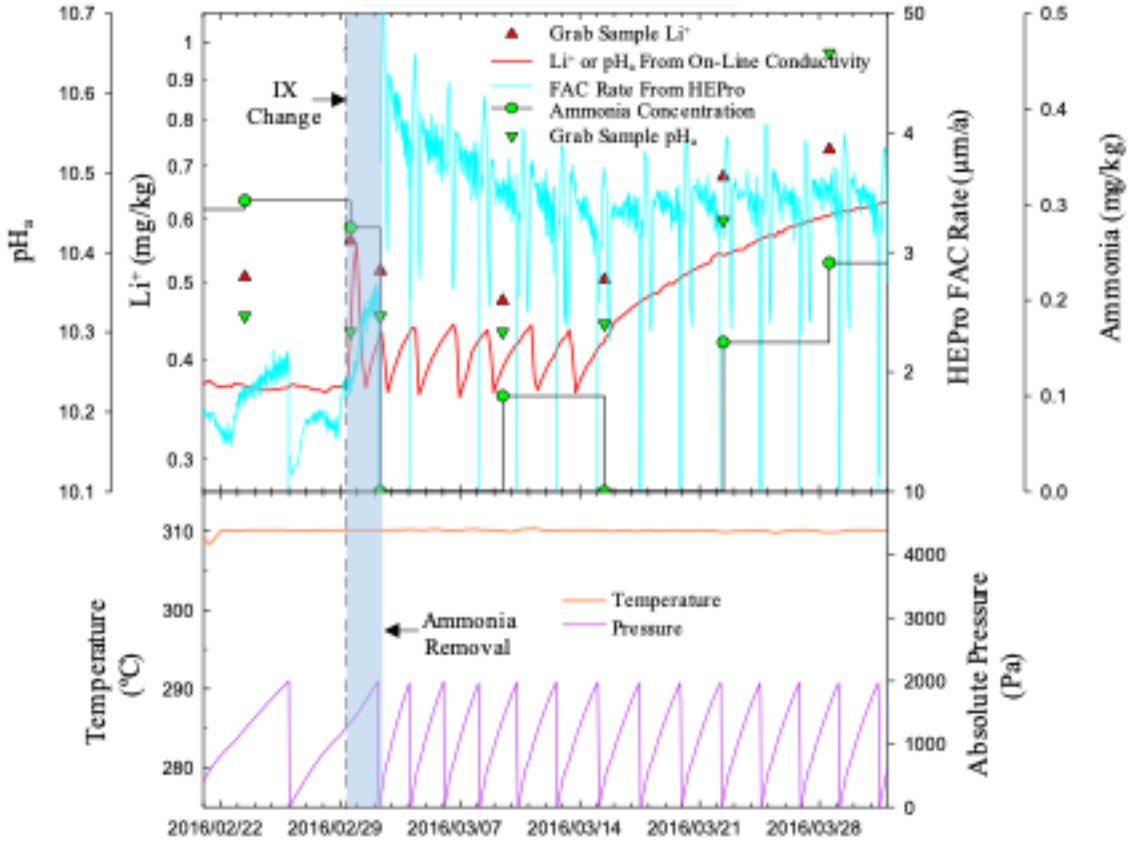

Figure 2.4-1 2016 Observed PHTS Chemistry

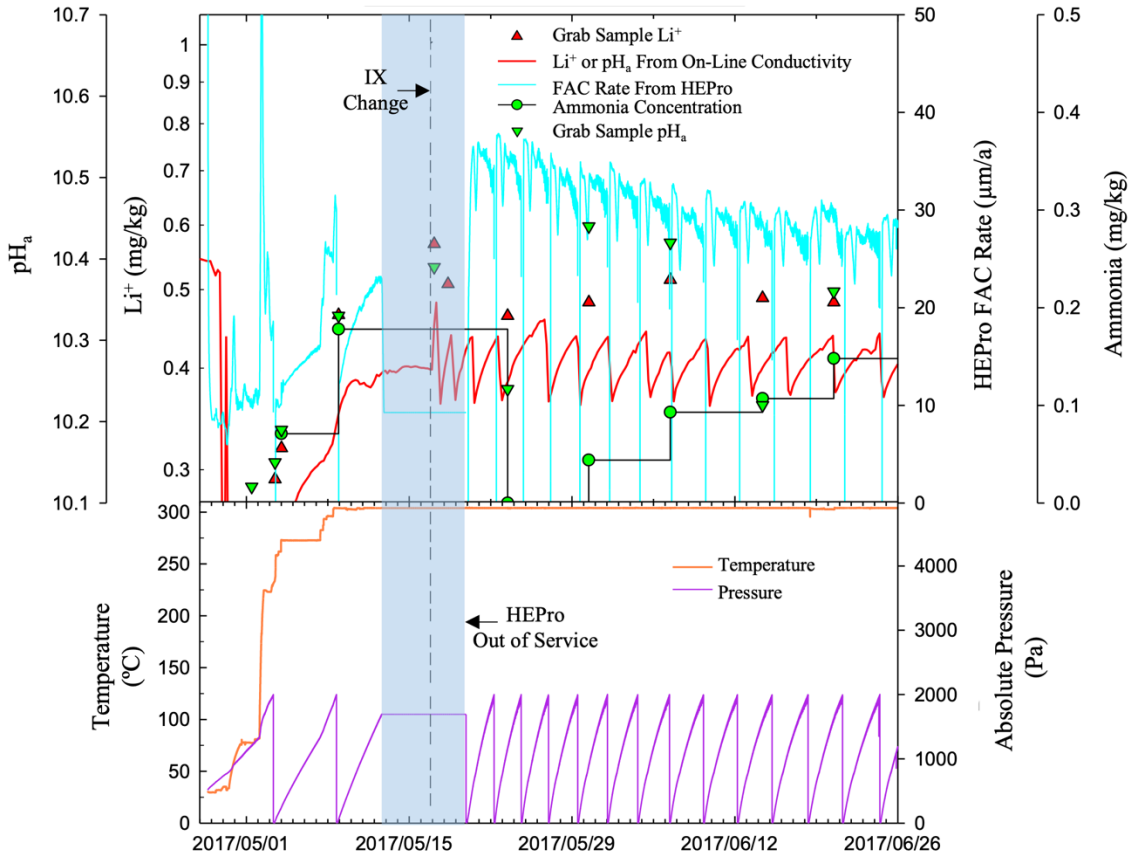

Figure 2.4-2 2017 Observed PHTS Chemistry

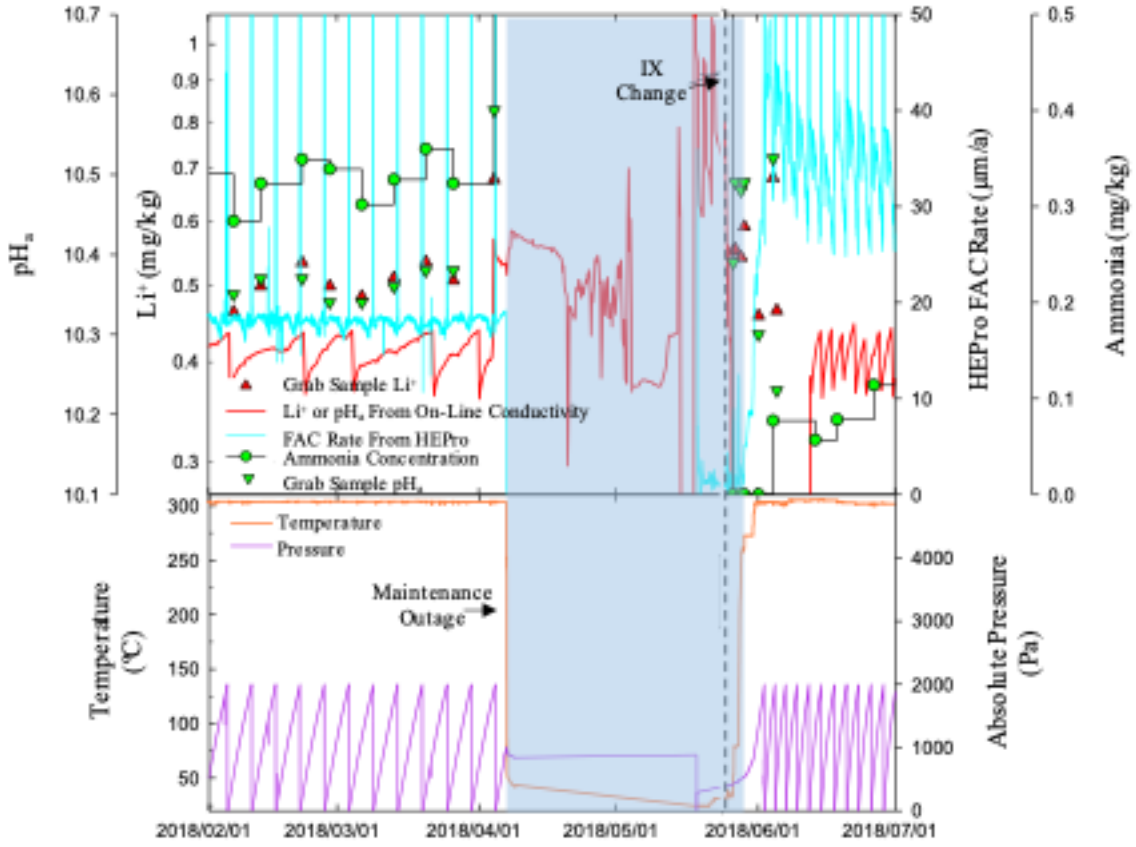

Figure 2.4-3 2018 Observed PHTS Chemistry.

Pre-refurbishment HEPro and PHTS chemistry data were acquired to investigate if this phenomenon is consistent over the life of the PLNGS CANDU unit. During refurbishment, the A106B carbon steel HTS feeders were replaced with A106C material, which significantly reduced overall FAC rate in the HTS. As illustrated in Figure 2.4-4, the original HEPro at PLNGS observed an increased FAC rate of ~ 10 µm/yr following a resin change in 2007, demonstrating that this phenomenon was occurring prior to refurbishment.

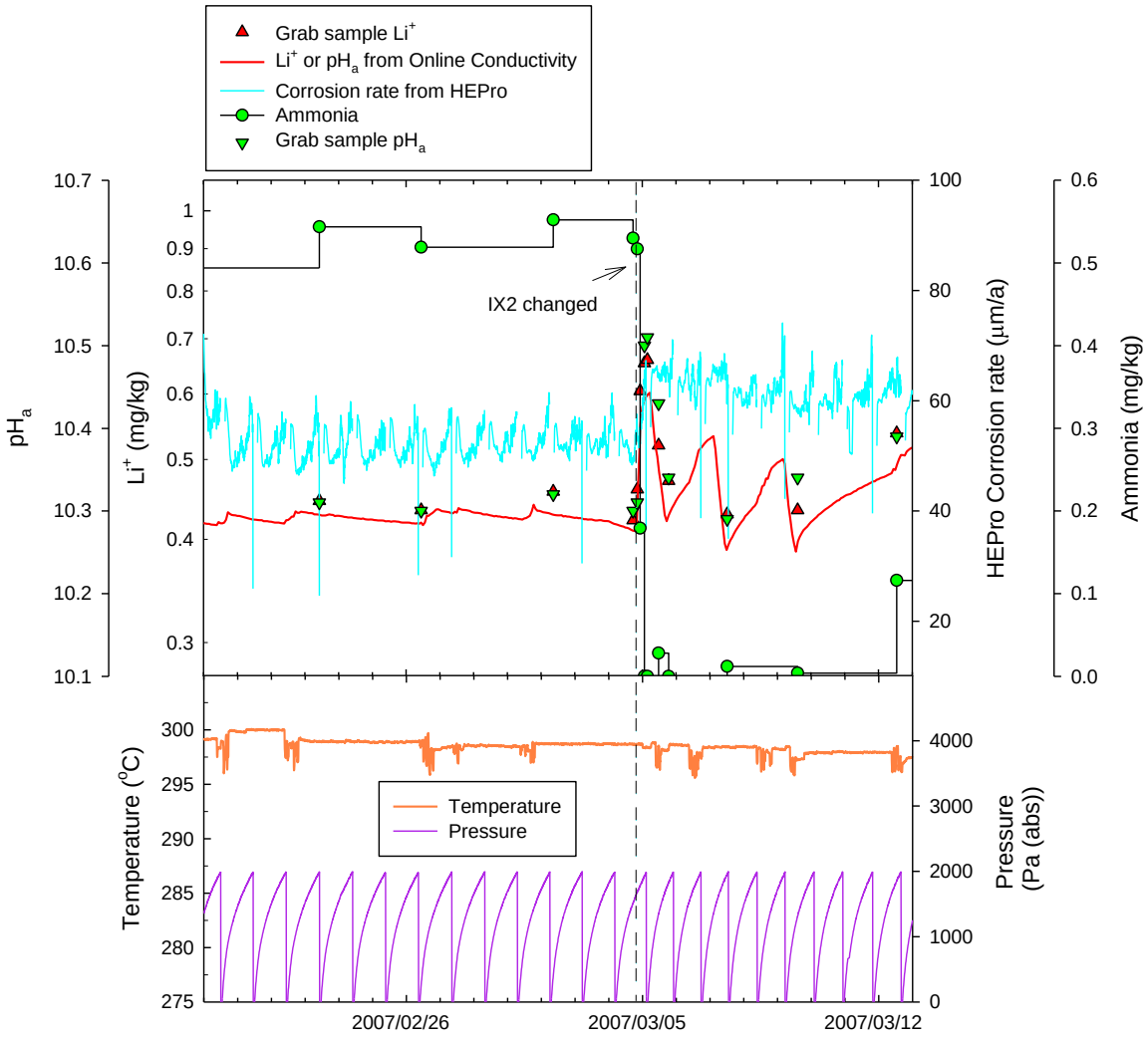

Figure 2.4-4. Derived FAC rate during the PHT IX resin change in March 2007 (pre-refurbishment).

Table 2.4-1 summarizes the observed concentration increase of lithium ions and FAC rate following IX resin change-out. On average, a rate of ~ 2.2×10^{-7} mol/kg/h of lithium was eluted from the IX resin. A theoretical ammonium production rate of ~ 5.3×10^{-9} mol/kg/h was inferred from radiolysis measurements. From Eq. 2.4-1 we know that the exchange of a lithium ion for an ammonium ion is one-to-one, while the exchange of lithium for iron is two-to-one (recall Eq. 2.1-6).

$$RLi + NH_4^+ \leftrightarrow RNH_4 + Li^+ \quad \text{Eq. 2.4-1}$$

Table 2.4-1 Lithium Concentration Increase

Date range	Average PHTS Li^+ increase rate (µg/kg/h)	Li^+ increase at IX outlet (mol/kg/h)	Derived Corrosion rates (µm/a)		
			Before	After	Delta
Mar 4th-16th, 2016	1.61	2.67×10^{-7}	18	37	19
May 18th - Jun 4th, 2017	1.50	2.67×10^{-7}	19	35	16
Jun 15th – Jul 2nd, 2018	1.42	2.33×10^{-7}	19	34	15
Average	1.51	2.20×10^{-7}	18.7	35.3	16.7

Given that ammonium and iron are the only cations of significant quantity present in the PHTS (other than lithium), it is assumed that the removal of ammonium must account for ~ 5.3×10^{-9} mol/kg/h of the calculated lithium eluted, and iron must account for the remaining ~ 2.12×10^{-7} mol/kg/h of eluted lithium. This equates to ~ 1.06×10^{-7} mol/kg/h of iron removed, which as shown in Figure 2.4-5, is almost an order of magnitude higher than the expected concentration of iron in the system, according to the Tremaine and Leblanc iron solubility data [3]. It is, however, within the solubility limit of the data reported by Sweeton and Baes [26].

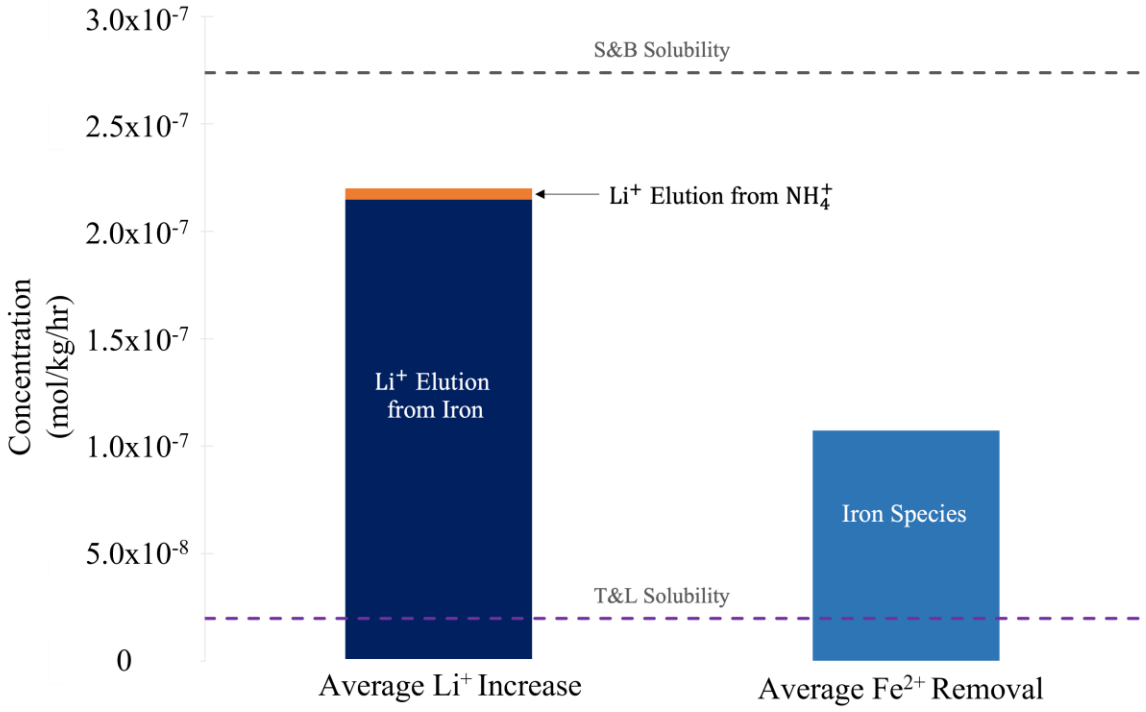

Figure 2.4-5. Lithium Eluted and Iron Removal Following IX Resin Change-Out. [3] [26]

Various computer models have been developed in an effort to predict the corrosion rate in the PHTS outlet feeders, including the CNER model which was first developed in the 1990's. Since its initial conception, the CNER model has been continuously updated and modified to predict activity transport, corrosion product deposition profiles and more accurately model how the operation of the purification system influences the iron concentration in the bulk fluid. More recently, the CNER model has been modified to utilize the Sweeton and Baes [26] magnetite solubility data, rather than the data reported by Tremaine and Leblanc magnetite solubility data [3]. Aligning with the data given in Figure 2.4-5, the Tremaine and Leblanc magnetite solubility data [3] fails to replicate the under-

saturation of iron experienced in the outlet feeder pipes. There is clearly more work to be done in understanding iron behaviour in the CANDU PHTS.

3 Experimental Methodology and System Design

3.1 FAC Experimental Test Loop and Test Plan

A discussed in Section 1, the objectives of this research are to demonstrate that the operation of the PHTS purification system has an impact on outlet feeder wall thinning; and more importantly, given this impact, determine strategies to optimize purification system operation and minimize FAC rate while still achieving purification efficacy for activity transport requirements.

The needs of this research called for a test loop that was not only capable of operating at CANDU PHTS conditions, but one that could facilitate continuous recirculation of the bulk process fluid and incorporate the controlled feed-and-bleed of a purification stream, all while monitoring corrosion in-situ and in real-time. In order to fulfil these objectives, CNER's Loop-1 was refurbished and modified to accommodate the needs of this research.

CNER's Loop-1 was originally designed to mimic the operational parameters of the CANDU PHTS, however it was not designed with a recirculating section on the "hot-side". Instead, the entire bulk fluid was heated, cooled, purified and returned to the reservoir with every pass, thus preventing an environment where dissolved corrosion products could accumulate, as in the CANDU PHTS. The system configuration of Loop-1, following modifications made during the first two years of this research (2018 – 2020), is detailed in the following sections. With the modifications and refurbishment of Loop-1 complete, experiments were begun in early March 2020 and continued until December 2020.

The test plan was formulated with the intent to observe how the corrosion of carbon steel test probes responded to varying purification flow rate, while the flow rate of the recirculating bulk fluid remains constant. Initial computational studies performed by CNER using the CNER FAC model suggested that the corrosion rate would vary as a function of purification rate, although the overall purification rates needed for the observed FAC increases were significantly higher than actually used in practice (i.e. 20% purification flow vs 0.5% in plant). Results from the computational study are given in Figure 3.1-1.

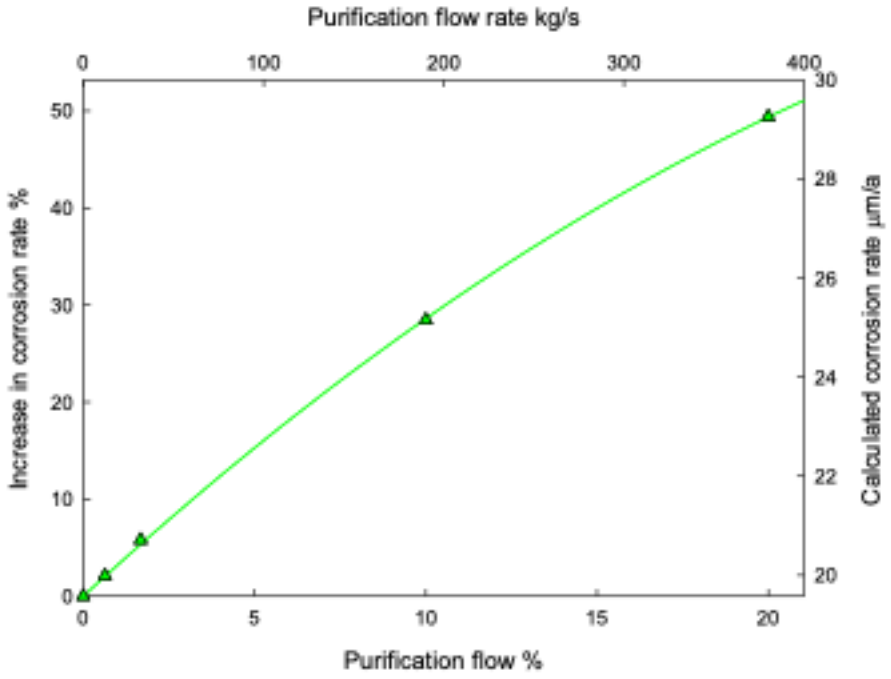

Figure 3.1-1. Computational Results for the Influence of IX Column Operation on FAC Rate.

During the initial development of the test plan, it was concluded that the most effective and accurate method to demonstrate the relationship between FAC and operation of the purification system would be to establish the minimum and maximum FAC rates achievable by the system — starting with the maximum rate, as operating experience

(OPEX) from CNER indicated that FAC may be difficult to initially induce. Establishing the maximum and minimum FAC boundaries is seemingly simple. All that is required to achieve the maximum FAC boundary is to operate Loop-1 with the highest purification rate that can be achieved by the system. Likewise, once sufficient data is collected, the purification rate may be decreased to the minimum rate that can be achieved by the system. Once boundaries are established, the experiment would then move onto increasing purification rate incrementally. Ideally, sacrificial carbon steel probes would be used to saturate the recirculating bulk fluid with iron for all trials — *with the exception of the first trial (trying to demonstrate maximum FAC rate)*. A complete test matrix describing the experimental plan is given in Table 3.1-1.

Table 3.1-1. Experimental Plan for FAC – IX Testing.

	Test Description	**Purification Flow Rate**	**Sacrificial CS**	**Expected Test Duration**
		mL/min (% Total)		**Weeks**
Test 1	Test commissioning, establish FAC	500 (25%)	N	2-4
Test 2	Minimum FAC rate establishment	20-50 (1-2.5%)	Y	2-4
Test 3	Determine dependence of FAC on increasing purification flow	100 (5%)	Y	1-2
Test 4		200 (10%)	Y	1-2
Test 5		300 (15%)	Y	1-2
Test 6		400 (20%)	Y	1-2
Test 7		500 (25%)	Y	1-2
Test 8	Verify consistent results	100 (5%)	Y	1-2
Test 9	Effect of IX resin change	TBD	Y	TBD
Test 10	35% anion augmentation	TBD	Y	TBD
Test 11	50% anion augmentation	TBD	Y	TBD

Table 3.1-2 gives targets for key operational parameters. Loop-1 is designed to operate with a recirculating section flow rate of ~ 2.9 LPM at 260 °C, which corresponds to a linear velocity across the corrosion probes of ~ 12 m/s. As with linear velocity, the other key operating parameters are also targeted the operating conditions observed in CANDU reactors.

Table 3.1-2 Targeted Key Operating Parameters.

Parameter	Value	Allowable Deviation
Temperature	310 °C	± 10 °C
Pressure (PT-3)	1500 psig	± 50 psig
$pH_{25°C}$	9.8	± 0.15
Flow Rates (FT-2)	2.9 L/min	± 0.9 L/min
Oxygen (O_2)	< 5 ppb	< 1 ppb ideal

While the test plan above is seemingly simple, various issues arose over the duration of this research which prevented the test plan from being carried out as described. The experiments performed and their associated results are discussed in detail in Section 4.

3.2 Configuration of LOOP-1 Following Modifications and Refurbishment

CNER's Loop-1 is designed to mimic the operating conditions of a typical CANDU-6 reactor. As previously discussed in Section 2.1.2, the absence of iron in the zirconium alloy fuel channels is a major contributing factor to the under-saturation of iron in the outlet feeder pipes, since the bulk fluid is unable to gradually acquire iron as its temperature increases along the reactor core. To mimic the absence of iron in the reactor

core, 316 stainless steel was selected as the primary material of construction for Loop-1 components. A brief schematic of Loop-1 is given in Figure 3-2. A detailed P&ID is located in Appendix D. Loop-1 is divided into two sections: a high-pressure side, and a low-pressure side.

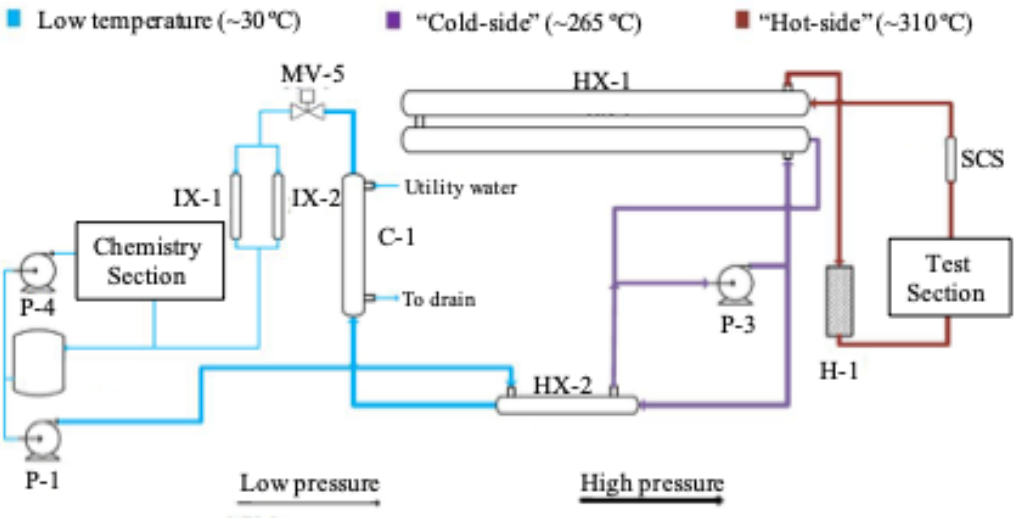

Figure 3.2-1. Simplified CNER Loop-1 Schematic Diagram.

The high-pressure section encompasses all components from the discharge of the positive-displacement pump (P-1) to the inlet of the pneumatic back-pressure regulating valve (MV-5) — it includes the low-pressure system feed-and-bleed, as well as a "recirculating-section" which has subsections referred to as the "hot-side" and the "cold-side" (refer to Figure 3-2). The cold-side operates at ~ 260 ºC and mimics conditions in the inlet feeders, while the hot-side operates at ~ 310 ºC and mimics conditions at the outlet feeders. The hot-side includes the test section for measuring FAC on typical A106B (or A106C) carbon steel, as well as a sacrificial carbon steel section, which is intended to help saturate the bulk fluid with aqueous iron.

The low-pressure section encompasses all components from the outlet of MV-5 to the suction side of P-1 — this includes the purification and chemistry monitoring sections, as well as the system reservoir (WT-1). The purification section is made up of a lithiated IX column (IX-1) and a hydrogenated IX column (IX-2). IX1 utilizes NRW37-Li resins (provided by PLNGS), while IX2 utilizes NRW37 resins.

3.2.1.1 High-Pressure Side

The bulk fluid is recirculated in the high-pressure section of the loop by a magnetically driven centrifugal pump (P-3). The bulk fluid flows through a single pass counter-current tube-in-tube heat-exchanger (HX-1), mimicking the heating and cooling processes of the reactor core and the steam generators. The discharge fluid from P-3 flows through a filter (F-3) and turbine flowmeter (FT-2)[12] prior to entering HX-1, mimicking the inlet feeders. The bulk fluid exits the HX-1 requiring additional thermal energy from the heater (H-1) to reach an operating temperature of ~ 310 ˚C.

The bulk fluid is then fed through the corrosion monitoring probes in the test section, or alternately the test section can be bypassed. To complete the figure-of-eight pattern of the PHTS, the bulk fluid can either be aligned with the sacrificial carbon steel (SCS) segment to increase the iron concentration in the bulk fluid or bypass the section prior to re-entering HX-1. The hot fluid exits HX-1. An additional single pass tube-in-tube cooler (C-2) was installed to allow for additional cooling should it be necessary. Note that C-2 is not included in Figure 3.2 as it was never utilized.

[12] See Appendix D for complete P&ID

3.2.1.2 Low-Pressure Side

A bleed stream to the low-pressure side (purification stream) is taken off the discharge side of P-3 (as is in the CANDU PHTS). Prior to being depressurized via MV-5, the purification stream gives its thermal energy to the feed stream from the discharge of P-1 via another single pass counter-current tube-in-tube heat-exchanger (HX-2). The purification stream is then further cooled to approximately 20 ˚C by a single-pass tube-in-tube cooler (C-1). Once cooled, the purification stream is filtered (F-1) to remove particulate corrosion products. The system is designed such that either IX column can be aligned to purify the stream of ionic impurities, or both IX columns can simply be bypassed. The stream is directed to the reservoir tank where the bulk process fluid chemistry is monitored and controlled.

The chemistry monitoring section draws its feed off the reservoir by a small magnetically driven centrifugal pump (P-4). The stream is filtered for any particulates that may be present in the fluid prior to the in-line pH probe and hydrogen and oxygen Orbispheres, which monitor the bulk fluid $pH_{25^{\circ}C}$, dissolved hydrogen and dissolved oxygen concentrations, respectively.

The pH of the bulk fluid is adjusted by either injecting a concentrated lithium hydroxide solution into the reservoir as a means of pH increase, or the pH of the bulk fluid can be reduced by aligning the purification stream with IX-2 (the H/OH mixed bed). The reservoir is equipped to continuously purge high purity hydrogen gas as a means to suppress the concentration of dissolved oxygen in the bulk fluid and to maintain reducing conditions in the process water.

3.3 **Corrosion Rate Measurements**

In the late 1990's, the UNB FAC program began developing in-situ and real-time corrosion monitoring techniques to observe how changing various operating parameters can influence the rate of FAC in the outlet feeders [25]. As of present, the CNER-UNB FAC program utilizes two corrosion probe monitoring techniques: the electrical resistance probe (ERP) and a lab scale HEPro – the hydrogen effusion probe (HEP). Although the premises of the ERP and the HEP differ, the fundamental design for both probe bodies is similar and is shown in Figure 3.3-1.

Figure 3.3-1. Schematic of Corrosion Probe Body.

The bodies of the probes are essentially designed as lab-scale outlet feeder pipes, where the inner and outer diameters are sized to generate a linear velocity of ~ 12 m/s under Loop-1 design parameters — approximately the same linear velocity that is experienced across some of the outlet feeders. The probes are machined in-house using feeder pipe material. The probes used in this research are machined from carbon steel A106C material, provided by the Darlington station. The probes are situated to operate in parallel of each other for data validation purposes. Table 3.3-1. gives the dimensions of the probe bodies.

Table 3.3-1. Corrosion Probe Dimensions.

	OD	**$OD_{Reduced}$**	**ID**	**$Length_{Total}$**	**$Length_{Reduced}$**
Inches	0.25	0.1559	0.063	3.17	0.392
mm	6.35	3.96	1.60	80.52	9.96

3.3.1 Electrical Resistance Probe (ERP)

The electrical resistance probe uses the principles of Ohm's Law to determine FAC rate — by incrementally measuring potential differential across two isolated points along the length of the probe and deriving resistance. The potential differential is measured across the length of the reduced section between the four silver wires shown in Figure 3.3-2. Heat shrink is applied to the surface area of the probe, on both sides of the reduced section and silver wires to maintain electrical isolation.

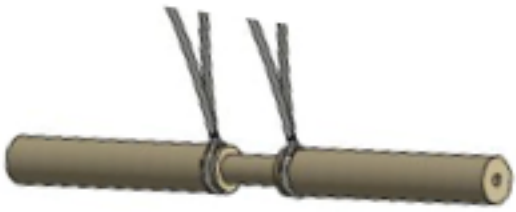

Figure 3.3-2. Schematic of the Electrical Resistance Probe (ERP).

Electrical resistance is dependent on the physical properties of the given material. As the inner surface of the probe corrodes the wall thickness decreases. Using Ohm's Law, we know that the electrical resistance (R) of the probe is equal to the product of the specific resistivity $(\rho(T))$ and the length of current flow (d), over its cross-sectional area (A_{Cross}), as per Eq. 3.3-1 [25]. Given that the specific resistivity of a material is temperature dependent, a temperature calibration was completed on the ERP during the final commissioning stages of Loop-1 (see Appendix B)

$$R = \frac{\rho(T) \cdot d}{A_{Cross}} \qquad \text{Eq. 3.3-1}$$

Knowing the outer radius (r_o) of the ERP reduced section, probe wall thickness (t_{wall}) can be derived using Eq. 3.3-2.

$$r_i = \sqrt{r_o^2 - \frac{\rho(T) \times d/\pi}{R}} \qquad \text{Eq. 3.3-2}$$

3.3.2 Hydrogen Effusion Probe (HEP)

As discussed previously in Section 2.2, in order to maintain charge neutrality the oxidation half-reaction of iron must be accompanied by a reduction half-reaction, where Eq. 2.2-1 and Eq. 2.2-2 are the oxidation and reduction half-reactions under reducing conditions it an iron-water system, respectively.

$$Fe_{(s)} \leftrightharpoons Fe^{2+}_{(aq)} + 2e^- \qquad \text{Eq. 2.2-1}$$

$$2H^+_{(aq)} + 2e^- \leftrightharpoons H_{2\,(g)} \qquad \text{Eq. 2.2-2}$$

The atomic hydrogen produced by the corrosion process *under reducing conditions* diffuses through the carbon steel pipe (or tube) to the exterior surface where it recombines to form hydrogen gas. Given that the oxidation of iron and the production of hydrogen gas are stoichiometrically equivalent, the corrosion rate can be determined by measuring the rate of hydrogen gas produced via pressure transducer. Figure 3.3-3 gives a schematic of the HEP, where a portion of the probe body is enclosed by an air-tight silver sleeve, thus trapping the hydrogen gas in an annulus region. Silver is the selected material for the sleeve given that its permeability to hydrogen is very low at high temperatures.

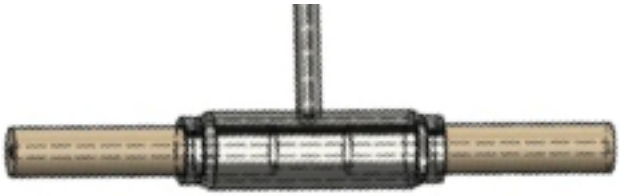

Figure 3.3-3. Schematic of Hydrogen Effusion Probe (HEP).

Figure 3.3-4 shows a schematic of all components required to capture and measure the hydrogen gas produced. The silver tube is soldered to a small opening on the silver sleeve, allowing hydrogen gas to distribute between the silver sleeve and pressure transducer. When the pressure in the HEP assembly is near maximum capacity, a vacuum pump is connected, and the hydrogen gas is evacuated.

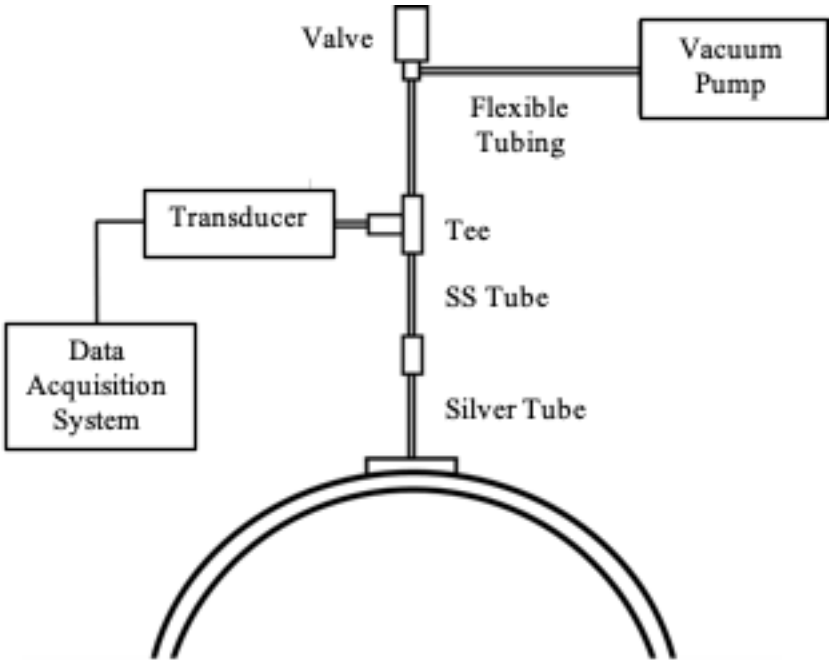

Figure 3.3-4. Schematic of HEPro Connections.

Given that the permeability of gas through metal is a function of temperature, the sections of the connecting tubes experiencing high temperatures must also be constructed with a metal that has low permeability to hydrogen at elevated temperatures, for sections at ambient temperature it is assumed that hydrogen absorption and diffusion through the tube materials is negligible. Table 3.3-2. gives the total enclosed volumes for the components in the "hot" and "cold" sections of the connection system.

Table 3.3-2. Connection System Component Volume.

Volume	m^3	cm^3
$\mathbf{Hot_{Total}}$	8.403×10^{-7}	0.840
$\mathbf{Cold_{Total}}$	3.315×10^{-6}	3.315
Total	4.155×10^{-6}	4.155
$\mathbf{Hot_{Frac}}$	0.202	

Since the chamber operates at low pressures and hydrogen is the only gas present, the hydrogen gas production rate can be simply derived by applying the Ideal Gas Law, as given in Eq. 3.3-3.

$$\frac{\delta n_{H_2}}{\delta t} = \frac{\delta P_{H_2}}{\delta t} \cdot \frac{V}{R \cdot T} \qquad \text{Eq. 3.3-3}$$

Where:

$\frac{\delta n_{H_2}}{\delta t}$ is the production rate of hydrogen moles $\left(\frac{mol_{H_2}}{day}\right)$

$\frac{\delta P_{H_2}}{\delta t}$ is the production rate of hydrogen gas $\left(\frac{Pa}{day}\right)$

V is the volume of hydrogen gas (m^3)

R is the Ideal Gas Constant $\left(8.314 \frac{m^3 \cdot Pa}{mol \cdot K}\right)$

T is the temperature of the hydrogen gas (K)

Again, because the oxidation of iron and the production of hydrogen gas are stoichiometrically equivalent, FAC rate can be calculated by Eq. 3.3-4, where the diffusion area for hydrogen through the carbon steel, iron density and molecular weight are constant as shown below.

$$\dot{m} = \frac{\frac{\delta n_{H_2}}{\delta t} \cdot M_{Fe}}{A_{Diff} \cdot \rho_{Fe}} \qquad \text{Eq. 3.3-4}$$

Where:

M_{Fe} is the molecular weight of iron $\left(55.85\ \frac{g}{mol}\right)$

A_{Diff} is the diffusion area of hydrogen through carbon steel (cm^2)

ρ_{Fe} is the density of iron $\left(7.87\ \frac{g}{cm^3}\right)$

In order for the HEP to be a valid method of corrosion monitoring, the following conditions must be satisfied:

a) The stoichiometric factor relating the rate of atomic hydrogen production to the rate of iron atom oxidation is fixed, and is that defined by the following chemical reaction:

$$Fe + 2H^+ \rightarrow Fe^{2+} + 2H \qquad \text{Eq. 3.3-5}$$

b) All the atomic hydrogen produced by the FAC process is absorbed locally by the carbon steel experiencing FAC.

c) All the absorbed hydrogen diffuses through the wall of the carbon steel tube experiencing FAC, recombines to molecular hydrogen at the external interface, and passes into the gas phase in contact with the external surface.

d) Any molecular hydrogen dissolved in the electrolyte passing through the HEP does not contribute to the hydrogen flux through the wall of the probe.

In addition to the conditions given above, the HEP is *only a viable method of monitoring corrosion rate in a system operating under reducing conditions*, where the concentration of dissolved oxygen in the bulk fluid *must be less than 1-2 μg/kg (ppb)*. If the concentration of dissolved oxygen in the bulk fluid is higher than 1 μg/kg, the corrosion mechanism becomes Eq. 3.3-6.

$$2Fe_{(s)} + O_{2\,(aq)} + 2H_2O \rightarrow 2Fe^{2+}_{(aq)} + 4OH^- \qquad \text{Eq. 3.3-6}$$

4 Results and Discussion

4.1 Experiment 1

Experiment 1 began on March 18th, 2020 as UNB transitioned to only essential personnel on campus due to the first wave of the COVID-19 virus. Experiment 1 ran for ~ 62 days, where only two trials were able to be attempted. Average operating data for both trials is summarized in Table 4.1-1. As briefly discussed in Section 3.1, the corrosion probes were designed such that each would experience a linear velocity of ~ 12 m/s, requiring a recirculating section flow rate of 2.9 LPM. The highest recirculating flow rate achieved during Experiment 1 was 1.2 LPM, which equated to a linear velocity across the probes of 5.9 m/s. While a linear velocity of 5.9 m/s was not ideal, it was decided that the experiment would move forward regardless.

Table 4.1-1. Experiment 1 Average Operating Parameter Summary.

	Trial 1	**Trial 2**
Recirculating flow rate [L/min]	1.19	1.0
Purification Flow Rate [mL/min]	390.6	143.4
$pH_{25\ ^{\circ}C}$	10.7	10.9
Probe temp [°C]	305.2	304.8
Pump temp [°C]	217.4	238.2
Dissolved H_2 [ppm]	0.19	0.07
Dissolved O_2 [ppb]	25.1	44.1

The lower recirculating flow rates than expected were determined to be the consequence of pressure drop across the system, where tubing diameter expansions and

contractions at P-3 suction and discharge were significant contributors. Ultimately, it was also found that the 40 µm filter element in front of the magnetic flow meter in the high temperature section of the loop was clogged, contributing significantly to the overall pressure drop in the system. Given the inability of P-3 to withstand further pressure drop in the system, it was decided that the sacrificial carbon steel probes would not be utilized for any trial during experiments moving forward.

Figure 4.1-1 shows the calculated wall thickness for both corrosion probes used during the experiment, where the corrosion rate for the ERP and HEP are derived using the slope of ERP wall thickness and the rate of hydrogen gas production, respectively. The ERP reported a FAC rate of ~ 35 µm/a for Trial 1 while the HEP reported a corrosion rate of only ~ 8 µm/a.

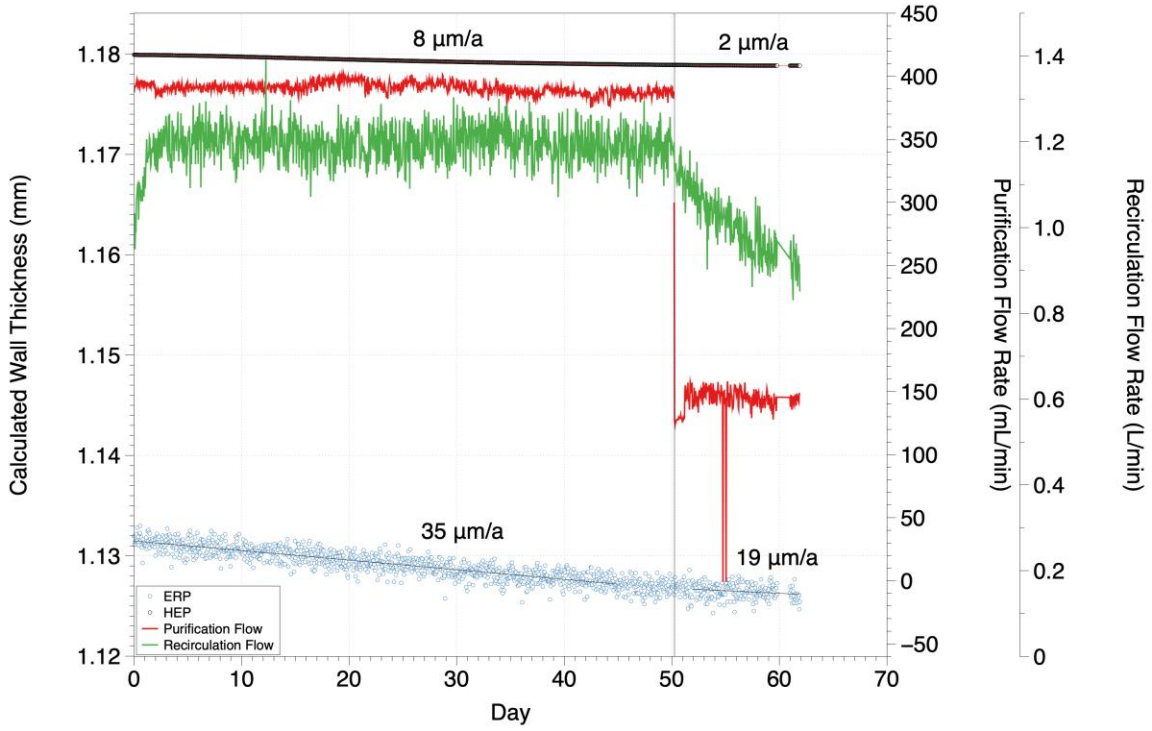

Figure 4.1-1. Experiment 1 Corrosion Probe and Flow Rate Data.

Figure 4.1-2 shows the data for the in-line pH and the concentrations of dissolved oxygen and hydrogen in the bulk fluid, measured via the online Orbispheres. The dissolved oxygen concentration remains fairly constant at ~ 20 ppb for 30 days prior to experiencing a significant step change around day 50 where it increased to about 30 ppb. The dissolved hydrogen remained < 1 ppm over the duration of the experiment.

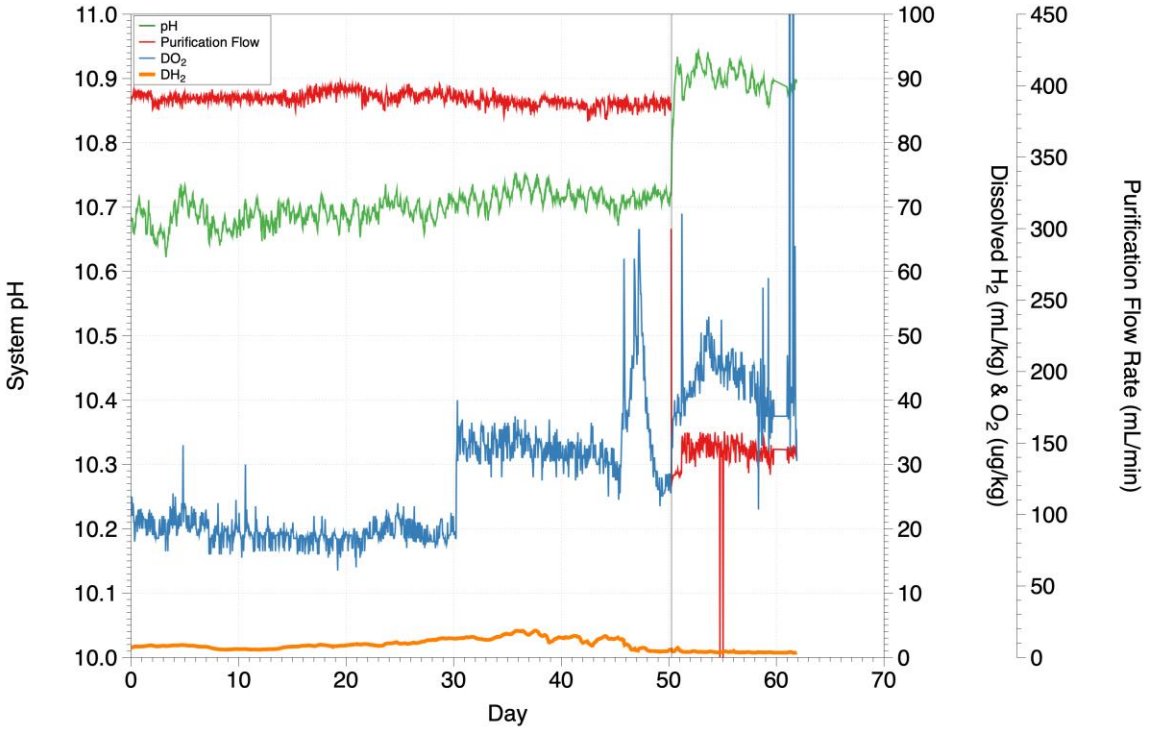

Figure 4.1-2. Experiment 1 Chemistry Data.

It is postulated that the FAC reported by the HEP (or lack thereof) is a consequence of high dissolved oxygen concentrations in the bulk fluid. As discussed in Section 3.3.2, the HEP is only suitable for corrosion monitoring under fully reducing conditions, where the concentration of dissolved oxygen in the system is ideally less than 1 ppb. As reported in Table 4.1-1., dissolved oxygen levels in the bulk fluid averaged 25.1 ppb and 44.1 ppb

for Trial 1 and Trial 2, respectively. Under these conditions, the oxidation of iron would occur by the oxygen reduction mechanism rather than hydrogen production.

As described in Section 3.1, the purpose of Trial 1 was to induce a maximum rate of FAC by operating with the highest purification rate achievable, while Trial 2 was designed to induce a minimum FAC rate by operating at the lowest possible purification flow rate, given that less dissolved iron is being removed from the recirculating bulk fluid. An immediate reduction in FAC rate reported by the ERP was observed from 35 μm/a to 19 μm/a when the purification rate was lowered from ~ 390 L/min to ~140 L/min on Day 50. A gradual reduction in recirculating flow rate was also observed following the reduction in the purification flow rate (see Figure 4.1-1). The reduction in recirculating flow rate was speculated to be the consequence of accumulated corrosion products on the filter (F-3) in that section of the loop, as it had been in place since commissioning and hadn't been serviced prior to starting the experiment. On Day 61, Loop-1 was shut down until it could be serviced in July, once students were allowed back on campus.

When removed for maintenance all three filters from Loop-1 showed startling amounts of magnetite deposits. Unfortunately, images and samples of the filters assessed from Experiment 1 were not retained, with the exception of the F-3 element from the recirculating section post cleaning. All filters were cleaned in a warm solution of dilute HCl in a sonicator bath. The filter from the high-temperature section was cleaned twice in but was ultimately replaced with a fresh 40 μm filter element.

Figure 4.1-3. Experiment 1 F-3 Post Cleaning.

As per Figure 4.1-2. and Table 4.1-1, the pH of the bulk fluid was significantly higher than the targeted pH. The high pH is a result of excess lithium hydroxide injected into the reservoir during lithiation of IX-1. Given that resources were limited during Experiment 1 due to the restrictions for on-campus activities, it was decided that the pH would be left as was, rather than to attempt to utilize the hydrogenated column to correct the pH. An interesting observation from Experiment 1 is the sudden pH increase following the transition to Trial 2. It is postulated that the increase in pH is a result of lithium elution from the IX column due to higher iron concentration in the recirculating section, similar to the observations from PLNGS.

4.2 Experiment 2

Experiment 2 commenced on July 17th, 2020 following the return of graduate students to the UNB Fredericton campus. Prior to beginning Experiment 2, activities entailed servicing the major loop components including the filters discussed in the previous section,

as well as the Orbispheres and in-line pH probe. The resin in IX-1 was replaced and the bulk pH was adjusted accordingly to the appropriate pH of 10.0. Average operating data for Experiment 2 is summarized in Table 4.2-1.

Table 4.2-1. Experiment 2 Average Operating Parameter Summary.

	Trial 1 (A)	**Trial 1 (B)**	**Trial 2**
Recirculating Flow Rate (L/min)	1.835	1.889	1.928
Purification Flow Rate (mL/min)	389.3	384.3	188.3
$pH_{In\text{-}Line}$	10.0	9.9	10.2
$pH_{Bench\ Top}$	9.99	10.05	10.08
Conductivity (µS/cm)	26.64	26.12	25.76
Probe temp (°C)	306.3	306.3	306.3
Pump temp (°C)	239.1	240.6	258.5
Dissolved H_2 (ppm)	0.1	2.0	1.6
Dissolved O_2 (ppb)	2.1	0.0	0.0

As shown in Figure 4.2-1., replacing the inline filter in front of the magnetic flow meter significantly increased the flowrate in the recirculating section from an average of ~ 1.2 L/min reported in Experiment 1 to approximately 2 L/min for Experiment 2. The increase in recirculating flow rate brought the linear velocity across the corrosion probes to ~ 9.7 m/s. Data from the ERP reported an FAC rate of 29 µm/a prior to an unplanned shutdown due to a brief power outage, while FAC along the HEP was not detectable.

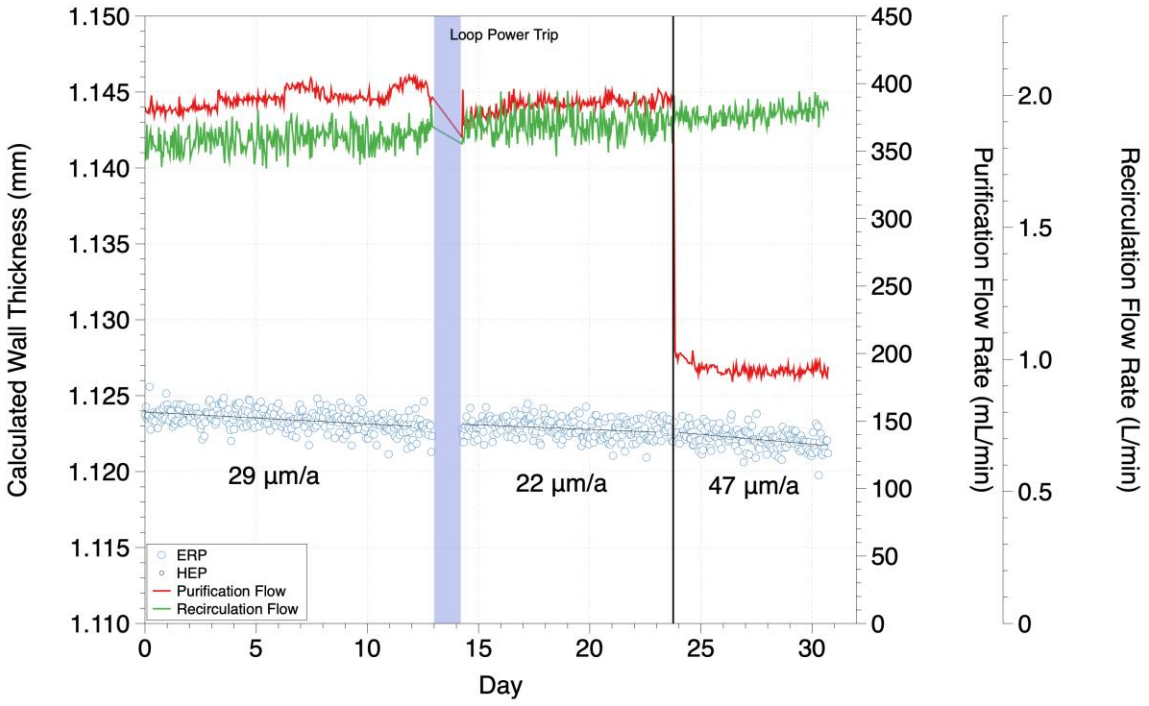

Figure 4.2-1. Experiment 2 Corrosion Probe Data.

Figure 4.2-2 gives the raw in-line pH, bench top pH, bench top conductivity, and Orbisphere data collected over the duration of Experiment 2. The dissolved oxygen concentration decreased to approximately 0 ppb within the first few days of operation, then fluctuated around the detection limit for the remainder of Experiment 2. As the dissolved oxygen measurements were dubious, the oxygen Orbisphere was serviced on Day 10, however, no changes in dissolved oxygen measurements were observed. The dissolved hydrogen measurements were also suspicious and remained near ~ 0 ppm until Loop-1 was restarted (Trial 1B) on Day 15 following a power outage that occurred on Day 13 at which point the measurements were about as expected given the equilibrium concentration of 18 mL/kg dissolved hydrogen with a pure hydrogen cover gas in the reservoir.

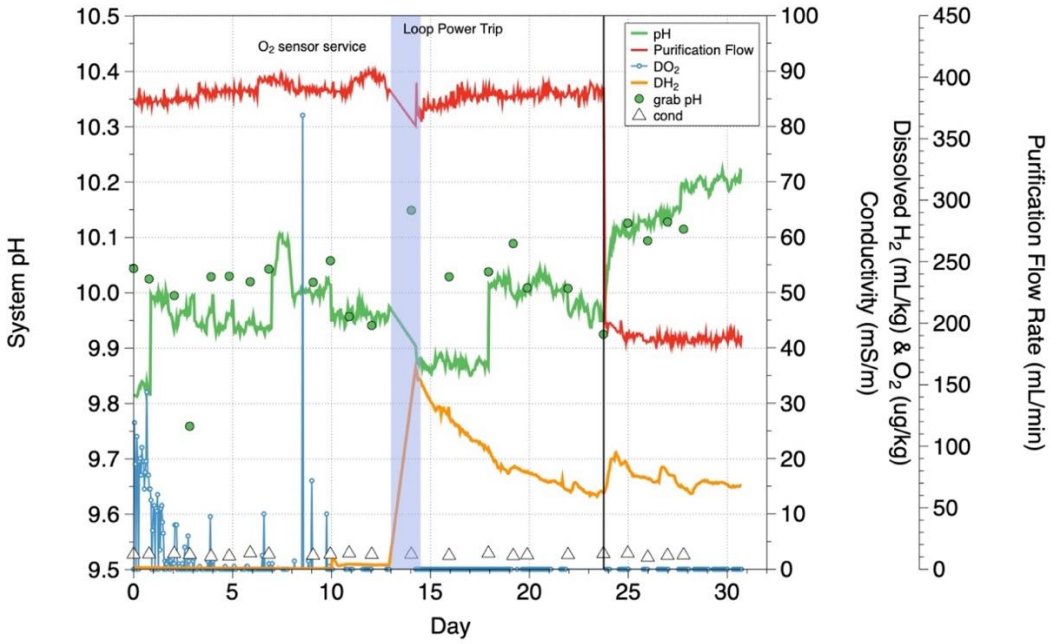

Figure 4.2-2. Experiment 2 Bulk Chemistry Data.

The lower corrosion rate demonstrated for Trial 1B (22 μm/a) versus Trial 1A (29 μm/a) is assumed to be a result of an increased iron content in the recirculating fluid. Loop trips and hot shutdowns are known to mobilize deposits, as such, it is expected that the mobilized corrosion products increased the concentration of iron in the recirculating bulk fluid. The filters in Loop-1 were serviced prior to starting up and continuing Trial 1 (Trial 1B) in order to mitigate the issues with increased pressure drop across F-3 (reduced recirculating flow rate) as result of corrosion product buildup. Figure 4.2-3. shows all the filters in Loop-1 prior to servicing activities. As illustrated in Figure 4.2-3., F-3 and the filter located upstream of the backpressure regulator (MV-5) showed a considerable amount of deposit, of what is most likely magnetite from its black appearance. All filters were cleaned in a warm solution of dilute HCl in a sonicator bath. Samples were not retained for quantifying the black deposits.

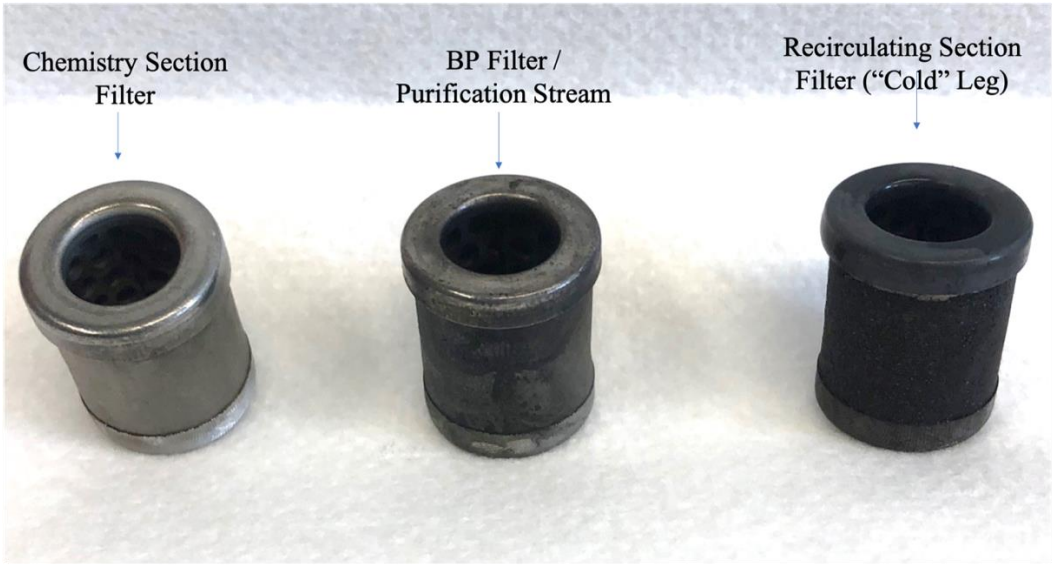

Figure 4.2-3. Filter Elements Following Hot Shutdown.

Despite lower concentrations of dissolved oxygen reported in the bulk fluid (~2.1 ppb for Trial 1A and below the detection limit for both Trial 1B and Trial 2) issues with the HEP continued into Experiment 2. After 10 days into Trial 1A the HEP pressure transducer was evacuated, and all associated HEP tubing was inspected in an effort to determine if the transducer/HEP was functioning properly — no abnormalities were identified. It is suspected that the dissolved oxygen concentration in the bulk fluid was still above the 1 ppb limit, these Orbisphere sensors are quite old and are difficult to ensure that they perform reliably. Given the lack of confidence in the dissolved oxygen measurements, the HEP was abandoned as a method of determining FAC rate and is not reported moving forward.

On Day 24, the purification flow rate was decreased from ~ 384 mL/min to ~ 188 mL/min. Following the decrease in purification flow rate, the rate of FAC observed by the ERP increased from ~ 22 μm/a in Trial 1B to ~ 47 μm/a in Trial 2. While this is the

opposite to what was anticipated, it is likely a result of inconsistent process conditions — specifically the bulk fluid pH and recirculating flow rate (linear velocity across corrosion probes). As shown in Figure 4.2-1. the flow rate in the purification system remains fairly constant at each setpoint, while the flow rate of the recirculating section increases slightly, but steadily over time. From Figure 2.3-3 we know that the solubility of iron increases with pH at elevated temperatures. It is possible that even a slight increase in both iron solubility and linear velocity across the corrosion probes could result in a significant increase in FAC rate. Approximately one week after switching to Trial 2, Loop-1 was forced to shut down on account of laboratory flooding caused by a blockage in the building service water drain line — utilized for C-1 cooling.

The reason for pH increasing following transition to Trial 2 is unknown. Figure 4.2-2. demonstrates a pH increase immediately following the transition from Trial 1B to Trial 2, averaging a pH value of ~ 9.9 and ~ 10.2, respectively, while Trial 1A averaged a pH of ~ 10, as per Table 4.2-1. To compensate for drifting pH readings, the in-line pH probe required a manual offset on Day 18 and regular grab samples were taken to confirm the in-line pH probe data. It is possible that the pH shift is a result of increased lithium elution due to iron uptake by IX-1, as mentioned above. Recall from Section 2.4, a similar trend was observed at PLNGS via in-line conductivity monitoring following IX resin changeout.

4.3 Experiment 3

Experiment 3 began once building service water drain line issues were resolved. Table 4.3-1. gives a summary of the average operating data for all six trials conducted during Experiment 3. Similar to the previous set of trials, all filters in Loop-1 were serviced

and cleaned prior to beginning Experiment 3 to mitigate pressure drop issues (decrease in flow rate) across the filter in the recirculating system (F-3).

Table 4.3-1. Experiment 3 Average Operating Parameter Summary.

	Trial 1A	**Trial 2**	**Trial 3A**	**Trial 3B**	**Trial 3C**	**Trial 1B**
Duration (day)	0 – 17	17 – 44	44 – 48	52 – 61	61 – 88	88 – 140
Purification flow rate (mL/min)	378.7	201.9	296.9	311.0	315.6	496.0
Recirculating flow rate (L/min)	1.9	2.0	2.0	1.3	2.0	2.0
$pH_{In\text{-}Line}$	10.05	10.17	10.12	10.11	10.10	10.11
$pH_{Bench\ Top}$	10.15	10.13	10.07	10.14	10.10	10.10
Conductivity (µS/cm)	23.48	31.89	37.62	32.07	29.11	36.38
Probe temp (°C)	306.1	306.0	306.0	303.3	306.0	291.7
Pump temp (°C)	239.4	255.8	246.6	221.7	244.6	217.3
Dissolved H_2 (ppm)	0.3	0.1	0.0	0.1	0.2	0.3
Dissolved O_2 (ppb)	0.0	0.0	0.0	27.4	64.0	1.2

Figure 4.3-1. shows the in-line pH, bench top pH, bench top conductivity, and Orbisphere data collected for Experiment 3. From Figure 4.3-1. and the average operating data presented in Table 4.3-1., it is observed that the pH remained fairly constant over the duration of the experiment. Unlike the observations made in Experiment 2, the pH did not increase following adjustments to the purification flow rate. Unfortunately, due to resource availability, grab samples were not able to be taken at the preferred frequency.

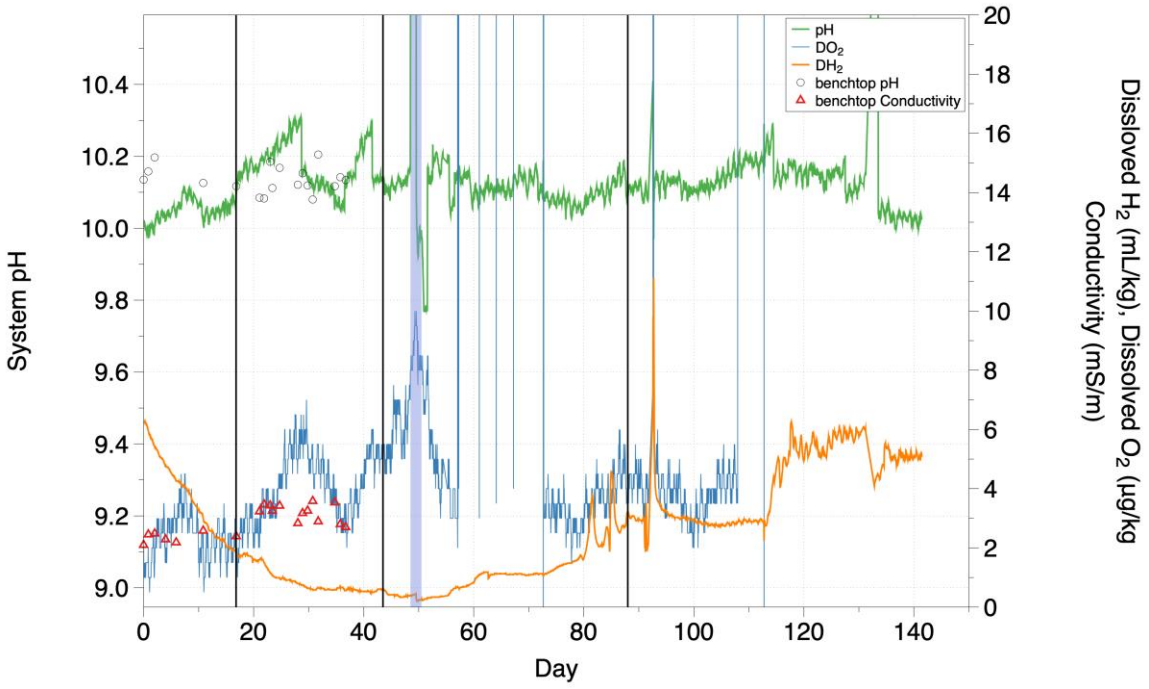

Figure 4.3-1. Experiment 3 pH and Conductivity Data.

The dissolved hydrogen concentration decreased from ~ 0.5 ppm to nearly 0 ppm over the course of Trial 1A and Trial 2 and begins to increase slightly near the end of Trial 3B. The dissolved oxygen concentration in the bulk fluid remains nearly 0 ppb until the concentration suddenly began to increase significantly to ~ 200 ppb just over midway through Trial 3B. The cause of the sudden increase of dissolved oxygen concentration was undetermined, however, it is expected that the Orbisphere sensor was malfunctioning.

Figure 4.3-2. shows the calculated ERP wall thickness, derived FAC rate, and the flow rates for both the recirculating and purification sections. While the HEP was kept inline to keep flow conditions consistent with the previous experiments (and also to avoid increased pressure drop across the system that would occur with a single probe aligned for

full flow) data from the HEP is not reported due to its inability to produce a useful FAC rate at system operating conditions, as mentioned in the previous section.

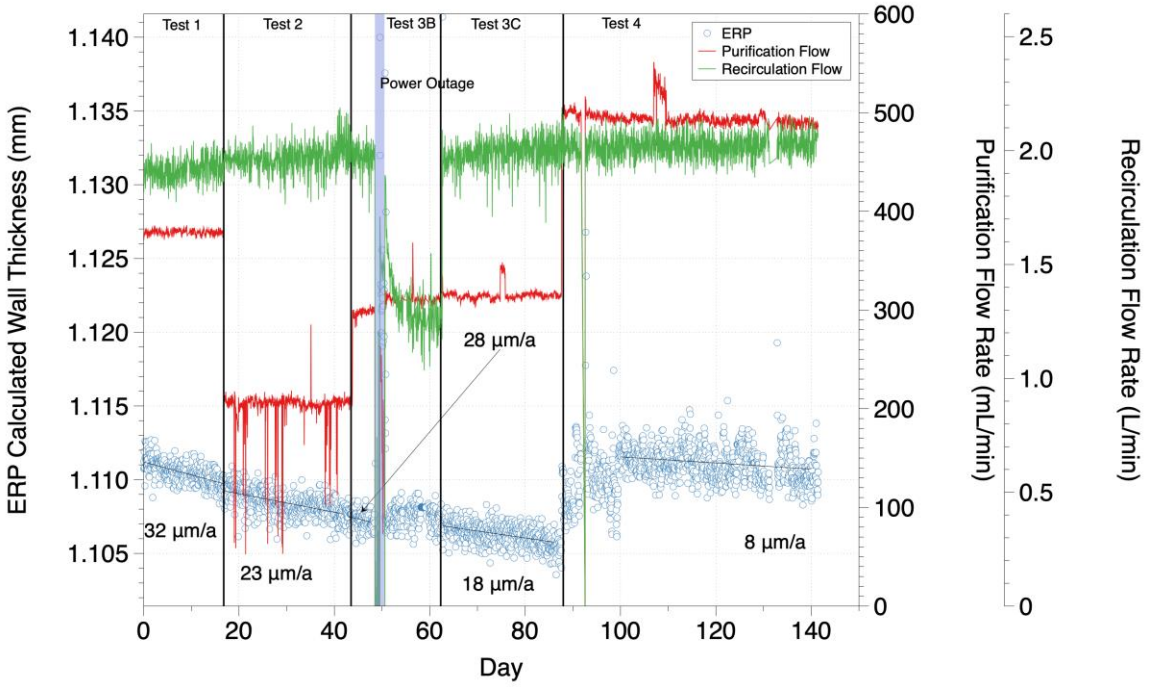

Figure 4.3-2. Experiment 3 Corrosion Probe Data.

As shown in Figure 4.3-2., a FAC rate of 32 µm/a was derived from the wall thickness data reported by the ERP for Trial 1A, which is consistent with the FAC rate derived in the previous trials for maximum purification flow rates. An FAC rate of 23 µm/a was derived using the ERP wall thickness data for Trial 2, following the decrease in purification flow rate from ~ 380 mL/min to ~ 200 mL/min on Day 17. On Day 44 the purification flow rate was increased to ~ 297 mL/min to observed how the rate of FAC varied with intermediate purification flow rates (Trial 3A). Loop-1 tripped only 4 days after switching to the intermediate purification flow rate. While the duration of Trial 3A did not allow

sufficient time for the FAC rate to fully stabilize, an FAC rate of 28 μm/a was estimated using linear regression.

Loop-1 was restarted immediately (on Day 50) in an attempt to continue the previous trial. However, in the haste to restart the experiment, the in-line filters were not cleaned, resulting in a decreasing recirculating flow rate. The loop was shut down briefly to service the filters and Trial 3C was started at an intermediate purification flow rate of ~ 300 mL/min on Day 62.

Figure 4.3-3 shows the filter elements from F-3 and F-1, respectively, following Trial 3B. Both filters, especially F-3, show a significant accumulation of magnetite deposits. An FAC rate of ~ 18 μm/a was derived for Trial 3C. It is suspected that the considerably lower FAC rate observed in Trial 3C (compared to Trial 3A) is a result of increased iron mobilization in the bulk fluid from the hot shutdown.

Figure 4.3-3. F-3 Element (left), F-1 Element (right).

On Day 87 the purification flow rate was increased to 500 mL/min in an attempt to accelerate the rate of iron removal from the system. Operating at a purification rate of ~ 500 mL/min resulted in decreased temperatures in the recirculating side of Loop-1 (Table 4.3-1) at the recirculating pump (P-3) and at the outlet of the test probes, which were reduced to 217.3 ℃ and 291.7 ℃, respectively. The decrease in operating temperature, coupled with the increased iron in the recirculating section resulted in a derived FAC rate of 8 μm/a. After several weeks of observing no change to FAC rate at these conditions, Loop-1 was shut down on Day 141 and Experiment 3 was terminated.

4.4 Discussion

As discussed in the three previous sections, many forced shutdowns were experienced over the course of this research — preventing the completion of the original test plan presented in Section 3. Fortunately, enough reproduceable data was collected from Experiment 1 and Experiment 3 to demonstrate that the rate of FAC is indeed influenced by the purification flow rate.

Table 4.4-1. presents a summary of data collected for trials that were not influenced by corrosion product mobilization due to a loop trip (hot shutdown), as it is suspected that the reduced FAC rates observed are a consequence of the increase of iron in the bulk fluid. As such, data for trials performed immediately following hot shutdowns were omitted given that: the driving force of FAC is a function of the difference between the iron-saturation concentration and the concentration of iron species in the bulk fluid (recall Eq. 2.3-1), thus a relatively consistent iron concentration in the bulk fluid is necessary for an accurate demonstration; and, increased iron due to mobilization is not consistent with the data reported from PLNGS in Section 2.4.

Table 4.4-1. Average Experimental Data Summary.

	FAC [μm/a]	Rec. flow [L/min]	Purf. flow [mL/min]	Lin. Velocity [m/s]	$pH_{25\,°C}$	Probe temp [ºC]	Pump temp [ºC]
Experiment 1 (Trial 1)	35	1.19	390	5.9	10.7	305	217
Experiment 1 (Trial 2)	19	1.0	143	5.1	10.9	304	238
Experiment 3 (Trial 1A)	32	1.9	378	9.7	10.05	306	239
Experiment 3 (Trial 2)	23	2.0	201	10.4	10.17	306	255
Experiment 3 (Trial 3A)	28	2.0	296	10.3	10.12	306	246

In addition to plotting the rate of FAC for each of the applicable trials from Experiment 1 and Experiment 3, as a function of purification flow rate (expressed as percent total flow of the circulating bulk fluid), Figure 4.4-1 also includes the CNER FAC modelling results presented in Figure 3.1-1.. The data presented demonstrates that the rate of FAC is in fact directly correlated to purification flow rate (percent total flow). Not only does the observed FAC rate increase as a function of purification flow rate for both experiments, but the slopes of both independent trials concur with 0.9 μm/yr per % increase in purification flow rate, despite the nearly doubled linear velocity across the ERP achieved in Experiment 3 versus Experiment 1. The difference between the FAC rates derived in Experiment 1 and Experiment 3 is likely due to the relationship between magnetite solubility and system pH, coupled with the slightly varied operating conditions for each experiment . Figure 4.4-2. utilizes the magnetite solubility data discussed in Section 2.3.2 to demonstrate how solubility bottoms out over a very narrow pH range and then increases rapidly when approaching slightly more acidic or alkaline conditions.

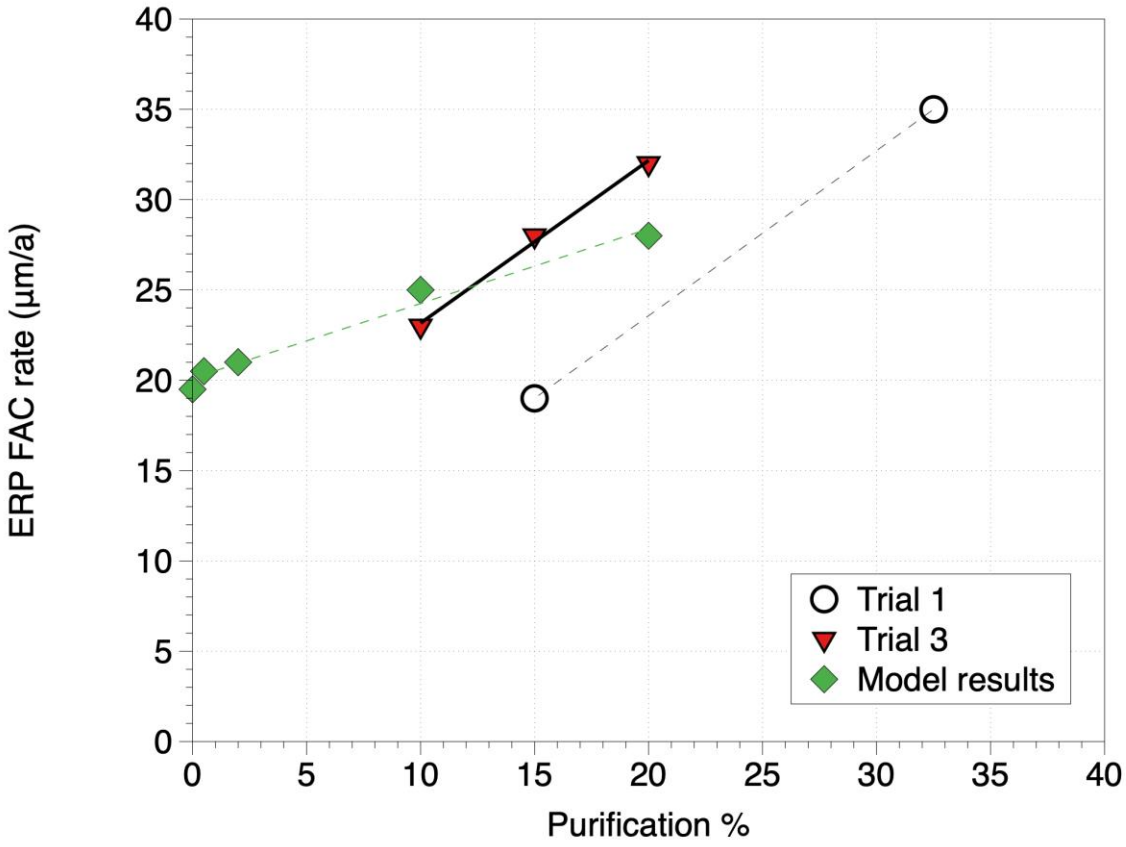

Figure 4.4-1 FAC rate on the ERP as a function of loop purification flow rate. Model results simulating CANDU-6 corrosion and purification rates are shown for comparison

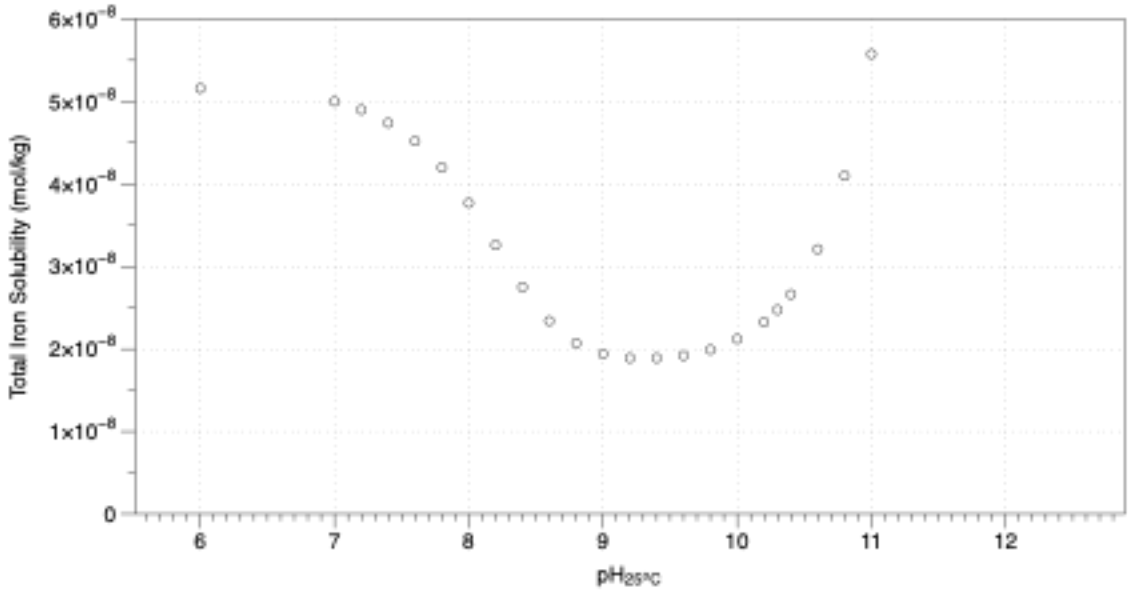

Figure 4.4-2. Solubility of Iron as a Function of pH at 310 ºC.

The CNER FAC model was developed specifically for simulating FAC rates in the PLNGS outlet feeders, where PLNGS operates with a purification flow rate nearing 0.5% total recirculating flow. FAC rates of ~ 29 μm/a and ~ 25 μm/a were computed assuming purification flow rates (percent of total recirculating flow) of 20% and 10%, respectively. While the CNER modelling results suggests there is less of a dependence on purification flow rate on FAC than what is observed from the experimental results, the modelling data concurs that there is in fact a direct relationship between the rate of FAC and the purification flow rate.

Given these observations, it is postulated that real HEPro data from PLNGS would demonstrate a greater influence of purification flow rate on derived FAC rates than what suggested by the CNER FAC model. This is expected given the small purification flow rate at PLNGS, in conjunction with: the reduction of iron removal as the resin becomes

saturated over time; iron speciation differences due to radiation fields in the reactor core; and potential increase of total iron solubility as a result of differing iron speciation.

Furthermore, parallel testing at CNER has demonstrated, with respect to mixed IX resin beds, that calculating FAC rates involves more variables than simply relying on the number of available exchange sites provided by the lithiated cation resins. The preliminary results from this testing program (see Appendix A) suggest that the anion resins in a mixed-bed (or the ratio of anion-to-cation resins) influences iron removal in the PHTS. Once the effect of anion-rich resins is well understood, it is reasonable to assume that the influence of purification flow on FAC at PLNGS can be scaled to other CANDU-6 units, which as discussed in Section 2.1.4 have differing anion resin capacities that vary by site.

5 Conclusions

In order to ensure optimal operation and longevity of both existing and future nuclear reactors, an in depth understanding of corrosion mechanisms is of the utmost importance. In CANDU systems, the $pH_{a,}$ is maintained such that it enables the formation of a protective oxide-film, while also minimizing the deposition of corrosion products that have potential to become activated as they migrate through the reactor core and the PHTS. In addition, purification systems, equipped with ion exchange resins, are utilized to further reduce potential activation and corrosion product deposition by simply removing aqueous corrosion products from the bulk fluid.

It has long been known that a metal's solubility and concentration in the bulk fluid play a significant role in various corrosion processes, particularly FAC. Despite this knowledge, the idea that the operation of the CANDU PHTS purification system (or removal rate of aqueous iron from bulk PHTS fluid) can significantly influence FAC in the outlet feeders never been considered.

PLNGS HEPro data from 2007, 2016, 2017, and 2018 presented in Section 2.4 demonstrate a clear correlation between operating with fresh IX resin and an increase in measured FAC rate. This correlation is further supported by initial computational studies using the CNER FAC model that relates purification flow rate to FAC rate.

Although there were numerous operational challenges over the course of this research, this work has achieved its primary objective by demonstrating that the operation of the purification system does in fact have an influence on FAC in the outlet feeder-pipes of CANDU reactors. Furthermore, it identifies that the effects for different units could be scalable providing the effects of anion-rich resin is determined.

6 Recommendations

The work presented in this thesis provides a strong foundation for further research regarding effect of purification flow rate on FAC in the outlet feeder pipes. Over the course of three years (2018 – 2021), much effort has been focused on modifying the existing Loop-1 at CNER to best simulate PHTS operational conditions at PLNGS, as well as gaining valuable experience on how to design and operate a system of this nature. It is recommended that Loop-1 be further modified into a concise modular configuration to limit pressure losses across the system and oxygen ingress, as well as updating the hydrogen and oxygen sensors with up-to-date models. The experiments presented in this thesis should be recreated with a smaller IX column to observe how the rate of FAC will be influenced as the resins approach/reach saturation conditions.

References

[1] World Nuclear Association, "World Nuclear Power Reactors & Uranium Requirements," May 2020. [Online]. Available: https://www.world-nuclear.org/information-library/facts-and-figures/world-nuclear-power-reactors-and-uranium-requireme.aspx. [Accessed April 2020]

[2] D. Lister and J. Slade, "The Accelerated Corrosion of CANDU Outlet Feeders - Observations, Possible Mechanisms and Potential Remedies," University of New Brunswick, Fredericton, 1997.

[3] P. Tremaine and J. LeBlanc, "The Solubility of Magnetite and the Hydrolysis and Oxidation of Ferrous in Water to 300C," Journal of Solution Chemistry, vol. 9, pp. 415-442, 1980.

[4] World Nuclear Association, "Nuclear Power Reactors," [Online]. Available: https://www.world-nuclear.org/information-library/nuclear-fuel-cycle/nuclear-power-reactors/nuclear-power-reactors.aspx. [Accessed February 2020]

[5] International Atomic Energy Agency, "Nuclear Power Reactors In The World," Reference Data Series No. 2, IAEA, Vienna (2019) [Online] Available: https://www.iaea.org/publications/13552/nuclear-power-reactors-in-the-world [Accessed April 2020]

[6] K. A. Burrill and E. L. Cheluget, "Corrosion of CANDU Outlet Feeder Pipes," Atomic Energy of Canada Limited, Canada, Tech. Report. AECL-11965; COG-98-292-I, 01 Feb 1999.

[7] W. G. Cook and C. Stuart, Flow Accelerated Corrosion at Point Lepreau Nuclear Generating Station, Frederiction, New Brunswick, 2018

[8] W. G. Cook, "HEPro and its Use at PLGS," Centre for Nuclear Research, Fredericton, 2016.

[9] The Essential CANDU, A Textbook on the CANDU Nuclear Power Plant Technology, Editor-in-Chief Wm. J. Garland, Chapter 6 Thermohydraulic Design, University Network of Excellence in Nuclear Engineering (UNENE), ISBN 0-9730040. Available: https://www.unene.ca/education/candu-textbook [Accessed April 2020]

[10] The Essential CANDU, A Textbook on the CANDU Nuclear Power Plant Technology, Editor-in-Chief Wm. J. Garland, Chapter 15 Nuclear Process Systems Chemistry and Corrosion, University Network of Excellence in Nuclear Engineering (UNENE), ISBN 0-9730040.Available: https://www.unene.ca/education/candu-textbook [Accessed April 2020]

[11] The Essential CANDU, A Textbook on the CANDU Nuclear Power Plant Technology, Editor-in-Chief Wm. J. Garland, Chapter 1 Introduction to Nuclear Reactors, University Network of Excellence in Nuclear Engineering (UNENE), ISBN 0-9730040. Available: https://www.unene.ca/education/candu-textbook [Accessed April 2020]

[12] World Nuclear Association, "Uranium Enrichment," [Online]. Available: https://www.world-nuclear.org/information-library/nuclear-fuel-cycle/conversion-enrichment-and-fabrication/uranium-enrichment.aspx. [Accessed January 2020]

[13] The Essential CANDU, A Textbook on the CANDU Nuclear Power Plant Technology, Editor-in-Chief Wm. J. Garland, Chapter 8 Plant Systems, University Network of Excellence in Nuclear Engineering (UNENE), ISBN 0-9730040. Available: https://www.unene.ca/education/candu-textbook [Accessed April 2020]

[14] The Essential CANDU, A Textbook on the CANDU Nuclear Power Plant Technology, Editor-in-Chief Wm. J. Garland, Chapter 2 Genealogy of CANDU Reactors, University Network of Excellence in Nuclear Engineering (UNENE), ISBN 0-9730040. Available: https://www.unene.ca/education/candu-textbook [Accessed April 2020]

[15] Lenntech " Purolite Resin NRW 37 Li7 Nuclear Grade Mixed Bed", [Online]. Available: https://www.lenntech.com/products/Purolite-Resin/NRW37Li7/NRW-37-Li7-Nuclear-Grade-Mixed-Bed/index.html#ixzz7eLcEZwGQ . [Accessed April 2020]

[16] Lenntech, "Fundamentals of Ion Exchange," 2000. [Online]. Available: https://www.lenntech.com/Data-sheets/Dowex-Ion-Exchange-Resins-Fundamentals-L.pdf [Accessed April 2020]

[17] C. E. Harland and R. W. Grimshaw, Ion Exchange : Theory and Practice, 2nd Edition ed., The Royal Society of Chemistry, 1994, p. 105.

[18] C. J. Geankoplis, "Chapter 12: Liquid-Liquid and Fluid-Solid Separation Processes," in Transport Processes and Separation Process Principles (Includes Unit Operations), Pearson, 2003, pp. 772-773.

[19] R. Akid, "Corrosion of Engineering Material," in Handbook of Advanced Materials: Enabling New Designs, J. K. Wessel, Ed., Hoboken, NJ: John Wiley & Sons, Inc, 2004, pp. 487-542.

[20] R. G. Mortimer, "Chapter 9: The Thermodynamics of Electrical Systems," in Physical Chemistry, 2 ed., Elsevier Science & Technology, 2000, pp. 297-299.

[21] R. P. Olive, "Pourbaix Diagrams, Solubility Predictions, and Corrosion Product Deposition Modelling For The Supercritical Water Reactor," University of New Brunswick, Fredericton, 2003.

[22] W. G. Cook, CHE 6714: Corrosion Processes and Pourbaix Diagrams, Fredericton, New Brunswick: University of New Brunswick, 2017.

[23] E. C. Potter and G. W. Mann, “Oxidation of Mild Steel in High-Temperature Aqueous Systems”, Proc. 1st International Congress on Metallic Corrosion, London. P. 417. 1961.

[24] O. Palazhchenko, CANDU Chemistry Course: General Chemistry Overview, Fredericton, New Brunswick: University of New Brunswick, 2020

[25] W. Cook, "Experiments and Models of General Corrosion and Flow-Assisted Corrosion of Materials in Nuclear Reactor Environments," University of New Brunswick, Fredericton, 2005.

[26] F. H. Sweeton and C. F. Baes, "The solubility of magnetite and hydrolysis of ferrous ion in aqueous solutions at elevated temperatures," The Journal of Chemical Thermodynamics, vol. 2, no. 4, pp. 479-500, July 1970.

[27] G. A. Kanert, G. W. Gray, and W. G. Baldwin, The Solubility of' Magnetite in Basic Solutions at Elevated Temperatures, Atomic Energy of Canada Ltd., Report AECL-5528 (1976).

[28] D. G. Miller and K. A. Burrill, "Characterization of oxides on Bruce "A" NGS liner tubes and steam generator tubes," in Corrosion 98 Conference, San Diego, CA, USA, 1998. Available from NACE International, P.O. Box 218340, Houston, TX 77218-8340

[29] V. S. Chew and F. R. Greening, "The effect of the CAN-DECON decontamination process on the surface oxides of Pickering units 1 & 2 feeder pipes," in Proceedings of the Canadian Nuclear Society Sixth Annual Conference, Ottawa, 1985.

[30] The Essential CANDU, A Textbook on the CANDU Nuclear Power Plant Technology, Editor-in-Chief Wm. J. Garland, Chapter 14 Nuclear Reactor Materials Chemistry and Corrosion, University Network of Excellence in Nuclear Engineering (UNENE), ISBN 0-9730040. Available: https://www.unene.ca/education/candu-textbook [Accessed April 2020]

Appendix A

Effects of Oxidizing Conditions on Iron-Saturated IX Resins

Redrafted after (*39th Annual CNS Conference & 43rd Annual CNS/CNA Student Conference*, June 2019)

EFFECTS OF OXIDIZING CONDITIONS ON IRON-SATURATED ION-EXCHANGE RESINS

J.A. Gauthier[1], J. Kongtuk[1], W.G. Cook[1], C.R. Stuart[2]

1. University of New Brunswick, Fredericton, New Brunswick, Canada (jessica.gauthier@unb.ca, jkongtuk@unb.ca, wcook@unb.ca)
2. Canadian Nuclear Laboratories, Chalk River, Ontario, Canada (craig.stuart@cnl.ca)

A Master's Level Submission

1. Introduction

This paper describes the results of a laboratory investigation examining the potential effects of oxidizing conditions on iron-saturated ion-exchange resins. Ion exchange is used in many process systems in the CANDU® reactor and oxidizing conditions may be present in certain operational scenarios such as a return-to-service of the primary heat transport system (PHTS) following a maintenance outage. The PHTS purification system in a CANDU® reactor is configured with dual beds: a lithiated mixed-bed ion-exchange column that serves to remove ionic impurities such as dissolved corrosion products and/or their activated counterparts (Co-60, Fe-59 etc.) and soluble fission products that may be in the system due to fuel failures; and a deuterated strong acid, strong base mixed bed to enable lithium removal and pH_a reduction. The strong acid cation resin exchanges either lithium or deuterium (dependent on which column is in operation) for ions with higher affinity for the resin, such as Fe^{2+} that is present in the system as dissolved iron. Examples of the exchange reactions are shown in Equations 1 and 2, where R represents a cation exchange site on the resin.

$$2\mathrm{RLi} + \mathrm{Fe}^{2+} \leftrightarrow 2\mathrm{R} - \mathrm{Fe} + 2\mathrm{Li}^{+} \quad (1)$$

$$2\mathrm{RD} + \mathrm{Fe}^{2+} \leftrightarrow 2\mathrm{R} - \mathrm{Fe} + 2\mathrm{D}^{+}, \quad (2)$$

It is postulated that under oxidizing conditions, such as those that may be present in the PHTS following a low-level drain state (LLDS) maintenance outage, the iron(II) compounds contained on iron-saturated resins may become oxidized to iron(III) precipitate compounds that are not retained on the resin exchange sites. The liberated exchange sites would then be available to remove Li^+ (and other cations) from the system. The removal of Li^+ would result in a water equilibrium shift and effectively bring the system to neutral pH_a conditions. The exact mechanism occurring is not yet understood , buta rudimentary chemical equation may be described as shown in Equation 3.

$$\mathrm{R}\cdot\mathrm{Fe(II)} + \mathrm{Li}^{+} + O_2 + H_2O \rightarrow \mathrm{R}\cdot\mathrm{Li} + \mathrm{Fe(III)}(OH)_x^n + H^{+} \quad (3)$$

Understanding of how an iron-saturated ion-exchange column behaves under oxidizing conditions offers valuable insights into the operational implications for CANDU® process systems such as the PHTS if the purification system were to be operated under such conditions.

2. Experimental methods

To ensure that the experimental results would be representative of plant operation, the Point Lepreau Nuclear Generating Station (PLNGS) provided a sample of their lithiated mixed bed resin (NRW37LiLC) that is used in the PHTS. Throughout the tests, the resin was contained in a ~ 20 mL stainless steel column and saturated with an iron sulphate stock solution. Once the saturation was achieved, a lithium hydroxide solution was pumped into the column, which was deaerated or aerated prior to injection. The pH of the column effluent was monitored online to observe the effect on the system conditions. Grab samples were taken at two minute intervals to measure the iron concentration through UV-vis spectrometry using the phenanthroline method [1]. All trials were preformed with light water solutions at room temperature.

2.1 Apparatus description

Figure 1 illustrates the apparatus used to perform the series of trials to investigate the effects of oxidizing conditions on iron-loaded mixed bed ion-exchange columns. Tank-1 contains the stock solution of [Fe^{2+}] (~0.008 mol/L – as ferrous sulphate heptahydrate mixed under a hydrogen atmosphere to ensure reducing conditions). The dissociation of the ferrous sulphate heptahydrate produced a slightly acidic stock solution, while this is not overly desired it was deemed acceptable for these tests to expedite the column saturation and avoid precipitation of iron hydroxides that would occur at elevated pH. Tank-2 and Tank-3 contain deaerated and aerated lithium hydroxide solutions, respectively, each with a pH of ~ 10.0. The preparation for each trial was extensive, requiring all deaerated stock solutions to purge with hydrogen overnight in a fume hood to ensure reducing conditions.

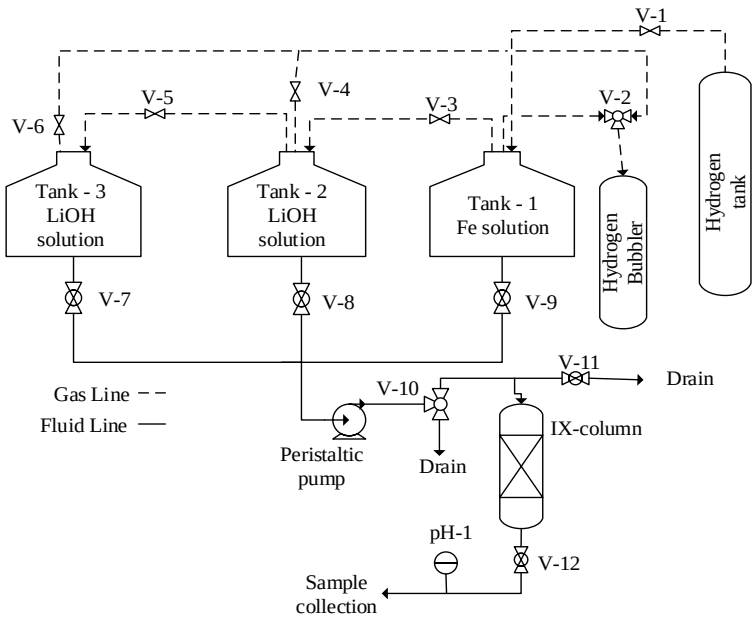

Figure 1: Diagram of ion-exchange apparatus.

The ion-exchange column was constructed using ~ 4" (10 cm) of 1/2" 316 stainless steel piping with a fine mesh screen at both ends to contain the resin. For each trial, the column was filled with approximately 11 grams of NRW37LiLC resin. A peristatic pump, operating at ~50 mL/min, was used to feed the column from each of the reservoirs. A 100 mL 3-neck flask was used to hold a bench-top pH probe (pH-1) downstream of the column outlet to monitor the effluent pH.

2.2 Experimental procedure

Each trial began by removing the air from the fresh ion-exchange resin by pumping in the deaerated lithium hydroxide solution from Tank-2. Once sufficient time had passed and no air bubbles were present in the column outlet stream, the peristaltic pump was changed to the iron stock solution, Tank-1. Injection of the iron solution continued until the ion-exchange resin was assumed saturated, based on preliminary saturation time calculations. The degree of ion-exchange saturation was later confirmed by comparing the concentration of the iron stock solution to the ion-exchange column effluent samples, via a UV-vis spectrophotometer, where the ion-exchange resin could be assumed saturated if the effluent concentration equalled that of the iron stock solution . Once the resin was assumed to be iron saturated, the peristaltic pump feed was changed to either the deaerated or aerated lithium hydroxide tank (Tank-2 or Tank-3). For each trial, grab samples were taken, mostly at two minute intervals, while a corresponding pH was recorded manually.

3. Experimental results and discussion

While multiple trials were conducted during the commissioning stages of these experiments, only the final few trials will be reported here and are shown in Table 1.

Table 1 Description of experimental trials

Trial	Description	Purpose
Trial 1	Fe-saturation then deaerated solution	Normal operation
Trial 2	Fe-saturation then aerated solution	Outage conditions
Trial 3	Fe-saturation deaerated then aerated solution	Transition to outage conditions
Trial 4	Partial Fe-saturation, repeat of Trial 3	Is the effect seen with partial resin saturation?

The results from Trial 1 and Trial 2, shown in Figure 2a and 2b, were conducted to observe how the iron-saturated resin would perform when fed a deaerated lithium hydroxide solution versus an aerated lithium hydroxide solution.

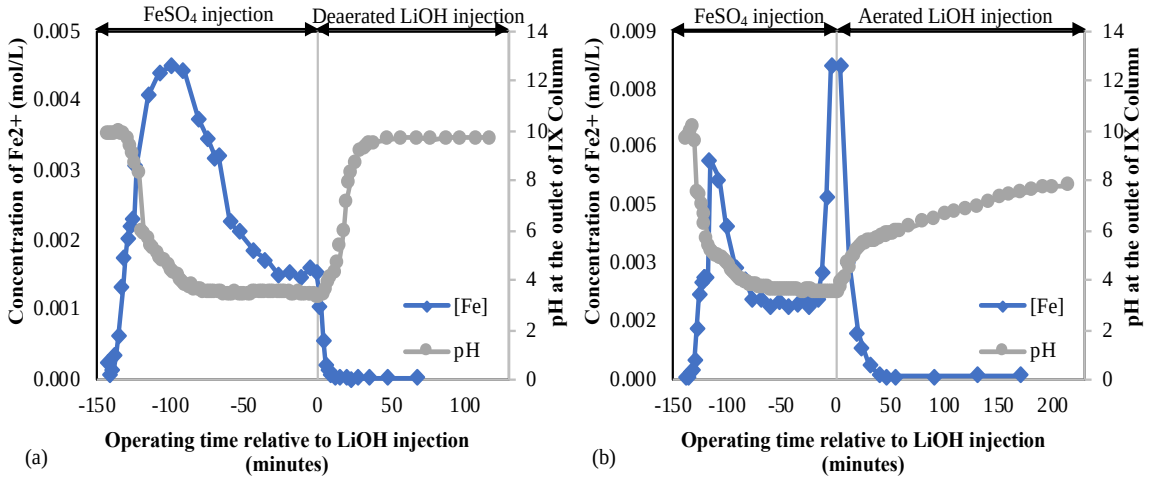

Figure 2 Fe^{2+} concentration and pH results from trial 1 (a) and trial 2 (b)

During the iron saturation stages of the trials, the pH of the ion-exchange column outlet fluid was consistent with the pH of the respective feed tanks. Following the iron saturation step for Trial 1 (Figure 2(a)), the ion-exchange column feed stock was switched to a deaerated lithium hydroxide solution (indicated as time-zero on the plot). This situation corresponds to the normal operation of the PHTS purification system where the fluid is typically fully deaerated. As shown in Figure 2(a), the pH of the ion-exchange column outlet stream increased nearly immediately when the feedstock was switched from the iron solution (pH $\approx$ 3.5) to the deaerated lithium hydroxide solution (pH $\approx$ 10). The relatively rapid pH stabilization suggests that the Li^+ passed directly through the column, as would be expected NRW37LiLC resins.

Trial 2 (Figure 2(b)) experienced a similar trend as observed in Trial 1 during the iron saturation segment of the experiment. However, once the feed to the ion-exchange column was changed to the aerated lithium hydroxide solution, the pH increased immediately but

only to neutral, and then only slowly increased towards a pH of approximately 10 over several hours. The immediate increase to neutral conditions, followed by a slow climb to a more alkaline pH suggests that the Li^+ were being removed from the lithium hydroxide feed solution. It is hypothesized that the Fe^{2+} initially absorbed on the resins precipitated under the oxidizing conditions, hence freeing exchange sites that then removed the Li^+. It is assumed that the pH would have continued to slowly increase until the ion-exchange resin saturation for Li^+ was reached. It is unclear why the iron concentration trends in both Trial 1 and Trial 2 increase and then decrease during the iron saturation stages. Unrefined analytical procedures and/or an aged source of ferrous sulphate heptahydrate are both plausible explanations.

Trial 3 and Trial 4 (Figure 3(a) and Figure 3(b)) demonstrate the performance of ion-exchange resin when it is fed deaerated and aerated lithium hydroxide solutions in sequence, where fully or partially iron-saturated resins were used, respectively. Trial 3 represents the system conditions of the PHTS that experiences oxygen ingress during a maintenance outage. As expected from the prior observations, the pH of the ion-exchange column effluent was consistent with that of the deaerated lithium hydroxide tank following iron saturation; however, once the ion-exchange column feed was switched to the aerated lithium hydroxide solution, the pH dropped to near neutral indicating Li^+ removal, as was observed in the prior testing. This confirms that the exposure of the resin to oxidizing conditions initiates the onset of lithium removal. It should be noted that Trial 3 and Trial 4 used a fresh source of ferrous sulphate heptahydrate, while Trial 1 and Trial 2 did not.

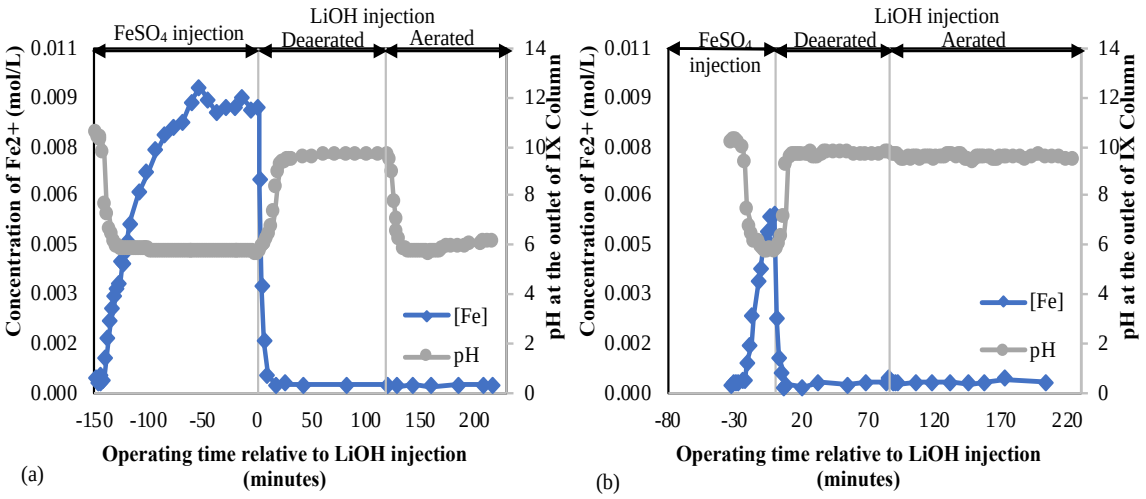

Figure 3 Fe^{2+} concentration and pH results from Trial 3 (a) and Trial 4 (b)

Trial 4 was performed using the same procedure and conditions as Trial 3, with the exception that the ion-exchange resin was only partially saturated with iron. The pH trend observed for Trial-4 behaved similarly to trend observed during Trial 3; however, after switching to the aerated tank, the pH remained steady at ~10 indicating no removal of the Li^+ from the solution. Results from Trial 4 suggest that ion-exchange beds that are not fully iron saturated will not cause a pH depression should oxidizing conditions arise.

4. Conclusions

In light of the experimental results, the following conclusions have been made:

- Exchange sites may become available when iron saturated resin is exposed to an oxidizing environment, resulting in lithium removal and pH depression.
- Fully and partially iron saturated resins perform differently when exposed to an oxidizing environment.

5. References

[1] ASTM Standard D1068, 2015, "Standard Test Methods for Iron in Water", ASTM International, West Conshohocken, PA, 2015, DOI: 10.1520/D1068-15, www.astm.org.

Appendix B

Electrical Resistance Probe Commissioning

As touched on in Section 3.3.1, given that the specific resistivity of a material is temperature dependent, a temperature calibration was completed on the ERP during the final commissioning stages of Loop-1. Following pressure tests, the ERP was installed in the thermally insulated test section and aligned in the flow path, with all heaters in the "OFF" position. The three "ON/OFF" heaters were then turned "ON". Once the temperature in the loop began to stabilize the controlling heaters were switched "ON" and the loop temperature was increased incrementally until the design temperature (310 °C) was reached. The flow rate of the bulk fluid was set low enough such that FAC would not occur, thus keeping the cross-sectional area constant. Results from the ERP temperature calibration are given in Figure A - 1.

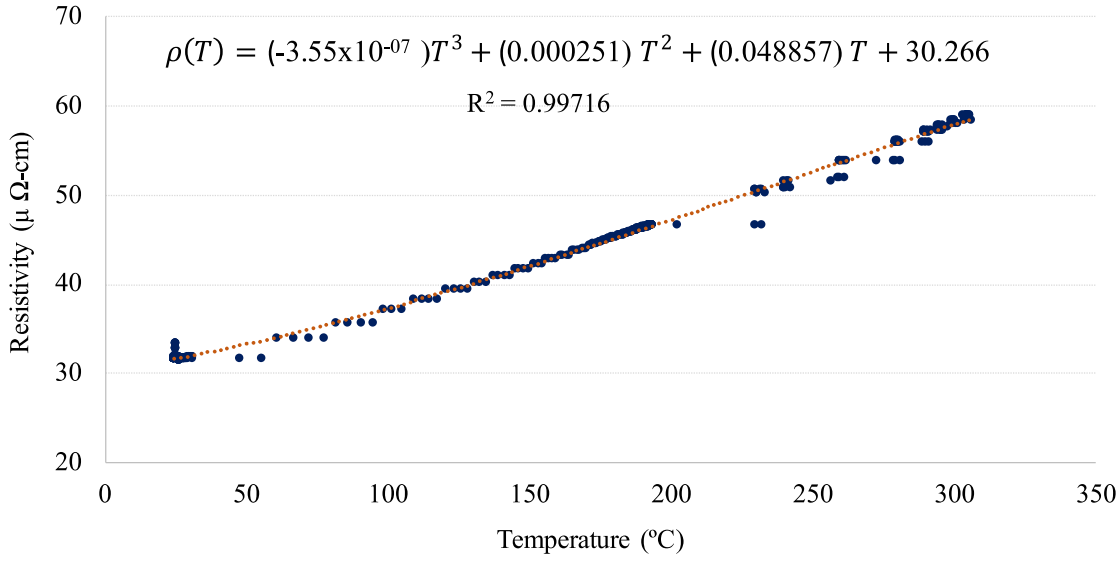

Figure A - 1 ERP calibration curve

Appendix C

Sample Calculations

Flow Accelerated Corrosion Rate on a ERP

Constants

$r_o = 1.979\ \text{mm}$

From raw data

$T_{Probe} = 305.1℃$

$R = 0.579\ \mu\Omega$

$\frac{dt_{wall}}{dt} = 9.55 \cdot 10^{-5}\ mm/a$

From ERP calibration (Figure A-1)

$$\rho(T) = -3.55 \cdot 10^{-10}(T_{Probe})^3 + 2.51 \cdot 10^{-7}(T_{Probe})^2 + 4.88 \cdot 10^{-5}(T_{Probe}) + 3.026 \cdot 10^{-2}$$

$$\rho(T) = -3.55 \cdot 10^{-10}(305.1)^3 + 2.51 \cdot 10^{-7}(305.1)^2 + 4.88 \cdot 10^{-5}(305.1) + 3.026 \cdot 10^{-2}$$

$$\rho(T) = 0.05846\ \mu\Omega - \text{cm}$$

Calculating wall thickness

$$t_{wall} = \sqrt{r_o^2 - \frac{\rho(T)\cdot(d/\pi)}{R}}$$

$$t_{wall} = \sqrt{(1.979\ mm)^2 - \frac{(0.05846\ \mu\Omega - \text{cm})\cdot\left(\frac{10\ mm}{1\ cm}\right)\cdot(9.95\ mm/\pi)}{0.579\ \mu\Omega}}$$

$$t_{wall} = 0.848\ \text{mm}$$

Comparing to original outer radius

$$t_{wall} = 1.979\ \text{mm} - 0.848\ \text{mm}$$

$$t_{wall} = 1.132\ \text{mm}$$

Calculating FAC rate

$$\dot{m} = \frac{dt_{wall}}{dt}\cdot\left(365\frac{day}{a}\right)\cdot\left(1000\frac{\mu m}{mm}\right)$$

$$\dot{m} = \left(9.55 \times 10^{-5}\frac{mm}{day}\right)\cdot\left(365\frac{day}{a}\right)\cdot\left(1000\frac{\mu m}{mm}\right)$$

$$\dot{m} = 34.85\frac{\mu m}{a}$$

Flow Accelerated Corrosion Rate on a HEP

Constants

$V_{Hot,fraction} = 0.202$

$V = 4.155 cm^3$

$A_{Diff} = 1.26\ cm^2$

Raw data

$T_{Probe,av} = 305.2$ ℃

$T_{Cold,av} = 26.5$ ℃

$\frac{\delta P_{H_2}}{\delta t} = 0.1273\ \frac{kPa}{day}$

Calculating effective temperature

$\mathrm{T}_{Eff} = \left(T_{Cold,av}\right) \cdot \left(1 - V_{Hot,fraction}\right) + \left(T_{Probe,av}\right) \cdot \left(V_{Hot,fraction}\right)$

$\mathrm{T}_{Eff} = (26.5\ ℃) \cdot (1 - 0.202) + (305.2\ ℃) \cdot (0.202)$

$\mathrm{T}_{Eff} = 82.82℃$

Calculating moles of hydrogen gas produced

$\frac{\delta n_{H_2}}{\delta t} = \frac{\delta P_{H_2}}{\delta t} \cdot \frac{V}{R \cdot \mathrm{T}_{Eff}}$

$\frac{\delta n_{H_2}}{\delta t} = \left(0.1273\ \frac{kPa}{day} \cdot \frac{10^3 Pa}{kPa}\right) \cdot \frac{4.155 cm^3}{\left(8.314 \frac{m^3 \cdot Pa}{mol \cdot K} \cdot \frac{10^6 cm^3}{m^3}\right) \cdot (355.97\ K)}$

$\frac{\delta n_{H_2}}{\delta t} = 1.789 \cdot 10^{-7}\ \frac{mol}{day}$

Calculating rate of FAC

$\dot{m} = \frac{\frac{\delta n_{H_2}}{\delta t} \cdot M_{Fe}}{A_{Diff} \cdot \rho_{Fe}}$

$\dot{m} = \frac{\left(1.789 \cdot 10^{-7} \frac{mol}{day} \cdot 365 \frac{days}{a}\right) \cdot (55.85\ g/mol)}{(1.26\ cm^2) \cdot (7.89\ g/cm^3)}$

$\dot{m} = 3.65 \cdot 10^{-4} \frac{cm}{a} \cdot \frac{10^4 \mu}{cm}$

$\dot{m} = 3.65\ \frac{\mu m}{a}$

Appendix D

Loop-1 Diagram

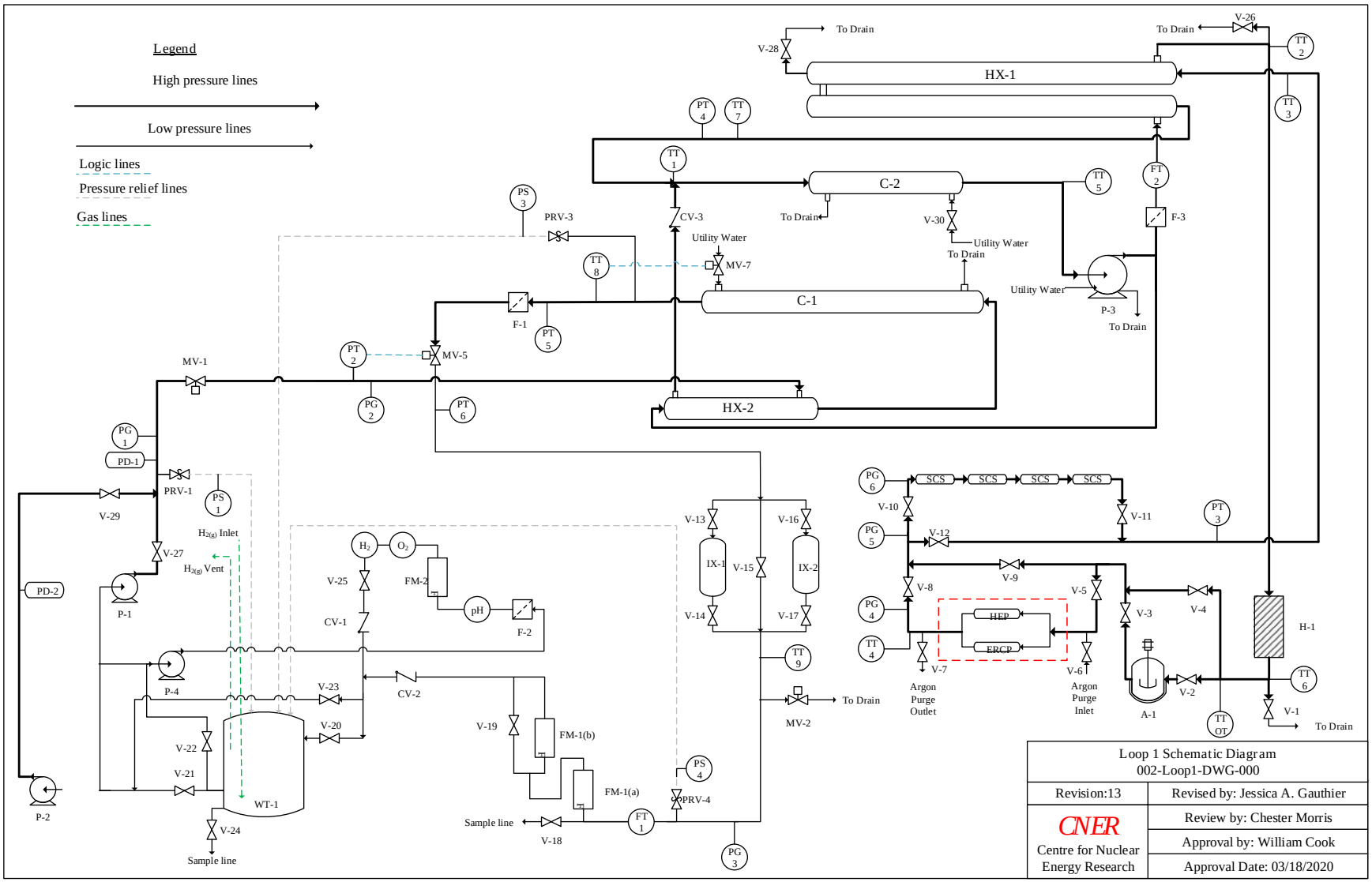
Legend
High pressure lines
Low pressure lines
Logic lines
Pressure relief lines
Gas lines
HX-1
HX-2
C-1
C-2
To Drain
Utility Water
Argon Purge Outlet
Argon Purge Inlet
Sample line
SCS
HEP
EPCP
Loop 1 Schematic Diagram
002-Loop1-DWG-000
Revision:13
Revised by: Jessica A. Gauthier
CNER
Centre for Nuclear Energy Research
Review by: Chester Morris
Approval by: William Cook
Approval Date: 03/18/2020

Curriculum Vitae

Candidate's full name: Jessica Ashley Gauthier

Universities attended (with dates and degrees obtained):

University of New Brunswick
Degree Information: BScE in Chemical Engineering
Completed: December 2017

Publications:

"EFFECTS OF PURIFICATION FLOW RATE ON FAC IN THE PHTS", Paper accepted to the *40th Annual CNS Conference & 44th Annual CNS/CNA Student Conference*, June 2020.

"EFFECTS OF OXIDIZING CONDITIONS ON IRON-SATURATED ION-EXCHANGE RESINS", Contributing author for paper accepted to the *39th Annual CNS Conference & 43rd Annual CNS/CNA Student Conference*, June 2019.

Conference Presentations:

"EFFECTS OF PURIFICATION FLOW RATE ON FAC IN THE PHTS", Poster presented at the *40th Annual CNS Conference & 44th Annual CNS/CNA Student Conference*, June 2020.

"EFFECTS OF PURIFICATION FLOW RATE ON FAC IN THE PHTS", Poster presented at the *University Network of Excellence in Nuclear Engineering (UNENE)'s R&D Workshop*, December 2019,

"EFFECTS OF OXIDIZING CONDITIONS ON IRON-SATURATED ION-EXCHANGE RESINS", Poster presented at the *39th Annual CNS Conference & 43rd Annual CNS/CNA Student Conference*, June 2019.